



AMERICAN METEOROLOGICAL SOCIETY

Journal of Climate

EARLY ONLINE RELEASE

This is a preliminary PDF of the author-produced manuscript that has been peer-reviewed and accepted for publication. Since it is being posted so soon after acceptance, it has not yet been copyedited, formatted, or processed by AMS Publications. This preliminary version of the manuscript may be downloaded, distributed, and cited, but please be aware that there will be visual differences and possibly some content differences between this version and the final published version.

The DOI for this manuscript is doi: 10.1175/JCLI-D-17-0064.1

The final published version of this manuscript will replace the preliminary version at the above DOI once it is available.

If you would like to cite this EOR in a separate work, please use the following full citation:

Deng, K., S. Yang, M. Ting, C. Hu, and M. Lu, 2017: Variations of Mid-Pacific Trough and Their Relations to the Asian-Pacific-North American Climate: Roles of Tropical Sea Surface Temperature and Arctic Sea Ice. *J. Climate*. doi:10.1175/JCLI-D-17-0064.1, in press.

Abstract

23

24 The mid-Pacific trough (MPT), occurring in the upper troposphere during boreal summer,
25 acts as an atmospheric bridge connecting the climate variations over Asia, the Pacific, and
26 North America. The first (second) mode of empirical orthogonal function analysis of the MPT,
27 which accounts for 20.3 (13.4) percent of the total variance, reflects a change in its intensity
28 on the southwestern (northeastern) portion of the trough. Both modes are significantly
29 correlated with the variability of tropical Pacific sea surface temperature (SST). Moreover,
30 the first mode is affected by Atlantic SST via planetary waves that originate from the North
31 Atlantic and propagate eastward across the Eurasian continent, and the second mode is
32 influenced by the Arctic sea ice near the Bering Strait by triggering an equatorward wave
33 train over the Northeast Pacific.

34 A stronger MPT shown in the first mode is significantly linked to drier and warmer
35 conditions in the Yangtze Basin, southern Japan, and northern U.S. and a wetter condition in
36 South Asia and northern China, while a stronger MPT shown in the second mode is
37 associated with drier and warmer southwestern U.S. In addition, an intensified MPT (no
38 matter in the southwestern or the northeastern portion) corresponds to more tropical cyclones
39 (TCs) over the western North Pacific (WNP) and less TCs over the eastern Pacific (EP) in
40 summer, which is associated with MPT-induced ascending and descending motions over the
41 WNP and the EP, respectively.

42 **1. Introduction**

43 The mid-Pacific trough (MPT) is one of the most prominent upper tropospheric
44 circulation features in the Northern Hemisphere (NH). It is also known as the tropical upper
45 tropospheric trough (Krishnamurti 1971; Sadler 1976, 1978) and the mid-oceanic trough over
46 the central Pacific (Colton 1973; Kousky and Gan 1981). The trough extends from the
47 mid-latitudes into the subtropics along a northeast-southwest direction (Sadler 1967) and
48 peaks in the upper troposphere during boreal summer. Although it is believed that the MPT
49 may be affected by many factors such as convection in the intertropical convergence zones
50 (Webster 1972; Hoskins and Rodwell 1995) and radiative cooling over the North Pacific
51 (Zhao et al. 2007), the exact mechanisms have never been fully understood.

52 The MPT can be decomposed into stationary and transient eddy parts (Ferreira and
53 Schubert 1999). The stationary part features a climatological appearance of the trough, while
54 the transient part refers to the synoptic-scale disturbances. Previous effort has been devoted to
55 investigations of the interaction between the MPT and tropical cyclones (TCs) (Kelley and
56 Mock 1982; Price and Vaughan 1992; Whitfield and Lyons 1992; Patla et al. 2009). On the
57 one hand, the MPT affects the origin and development of TCs by modifying the vertical wind
58 shear in which TCs are embedded (Gray 1968; Pfeffer and Challa 1992; Montgomery and
59 Farrell 1993; Hu et al. 2017). On the other hand, the MPT disturbances provide the initiation
60 to TCs by extending the trough into the middle-lower troposphere in some cases (Hodanish
61 and Gray 1993). In turn, TCs could also affect the MPT through Rossby wave energy
62 dispersion associated with the TCs (Ferreira and Schubert 1999). Patla et al. (2009) proposed

63 a conceptual model about how MPT influences TC tracks, offering a useful operational
64 guidance for weather forecasters. Recently, Wu et al. (2015) found that the MPT experienced
65 a pronounced westward shift during the past three decades in all of the available reanalysis
66 data sets, suppressing TC genesis in the eastern portion (east of 145°E) of the western North
67 Pacific due to the enhanced vertical wind shear associated with the MPT shift.

68 Moreover, the MPT can act as an atmospheric bridge connecting the eastern and western
69 hemispheres as well as tropical and extratropical regions. Recent studies have suggested
70 possible associations of the MPT with various atmospheric teleconnections. For example,
71 Zhang et al. (2005) noted that a stronger South Asian high (SAH) was accompanied by a
72 stronger and more extensive western North Pacific (WNP) subtropical high (WNPSH). The
73 enhancement and expansion of WNPSH could then push the MPT eastward, which
74 subsequently results in a stronger Mexican high. Thus, the MPT bridges the climate variations
75 in Asian-Pacific-American regions. In addition, as the MPT tilts along a southwest-northeast
76 direction over the subtropics, it could promote exchanges of heat and momentum between
77 different latitudes (Magaña and Yanai 1991; Waugh and Polvani 2000). Indeed, the MPT can
78 sometimes extend so far south into the tropics that the equatorial winds over the south of
79 MPT are switched from the trade easterlies to westerlies, forming the so-called equatorial
80 “westerly duct” that allows atmospheric disturbances to propagate from one hemisphere into
81 the other (Webster and Holton 1982; Webster and Yang 1989; Tomas and Webster 1994).

82 Therefore, understanding the variations and characteristics of the MPT is helpful for
83 untangling the interconnected weather events and climate anomalies in the

84 Asian-Pacific-North American regions. Although the synoptic features of the MPT and its
85 influence on TCs have been studied previously, the interannual and interdecadal variations of
86 the MPT and their climate impact are poorly understood so far. In fact, the MPT is often
87 regarded as a passive circulation feature induced from the upstream SAH, with its impact on
88 the climate in the remote regions being considered negligible. Given this belief, few studies
89 have been conducted about the multi-scale variations of the MPT, leaving an unanswered
90 question about the interannual variability of the MPT and its climate effect.

91 Given that the MPT connects the Asian and North American climate, as well as the
92 tropics and the mid-latitudes, the present study focuses on the interannual variation of MPT,
93 its possible effect on the Asian-Pacific-North American climate, and the responsible physical
94 mechanism. Although ENSO is the dominant mode of the climate variability in this region,
95 the ENSO alone could not fully explain the variability of MPT (Wang and Wu 2016). It is
96 important to seek and analyze other climate impacting factors for possible improvement over
97 the MPT-related climate forecasts.

98 The rest of the paper is organized as follows. Section 2 describes the data sets and
99 analysis methods applied. Section 3 discusses the climatological and interannual features of
100 the MPT. Sections 4 and 5 present the associated atmospheric circulation anomalies and
101 discuss the possible factors underlying the MPT variability. The effects of MPT on the
102 Asian-Pacific-North American climate are illustrated in section 6, followed by a summary
103 and a further discussion in section 7.

104 **2. Data and Method**

105 This study uses the monthly mean sea surface temperature (SST) data from the National
106 Oceanic and Atmospheric Administration (NOAA) extended reconstructed SST version 4
107 (Huang et al. 2015). The SST data set has a horizontal resolution of $2^{\circ}\times 2^{\circ}$ and is available
108 from 1854 to the present. The monthly precipitation data is obtained from the Global
109 Precipitation Climatology Center (GPCC, Schneider et al. 2011), with a horizontal resolution
110 of $1^{\circ}\times 1^{\circ}$ for the period of 1901-present. Surface air temperature anomalies are acquired from
111 the Goddard Institute for Space Studies (GISS/NASA), with a horizontal resolution of $2^{\circ}\times 2^{\circ}$
112 for the period of 1880-present. The monthly mean sea ice concentration data provided by
113 Japanese Reanalysis (JRA; Hirahara et al. 2014), with a horizontal resolution of $1^{\circ}\times 1^{\circ}$ for the
114 period of 1850-present, is available from the website at
115 <https://www.esrl.noaa.gov/psd/data/gridded/data.cobe2.html>. The JRA sea ice data merged
116 the satellite observations from the Nimbus-5 Scanning Multichannel Microwave Radiometer
117 (SMMR) from October 1978 to July 1987 and the Special Sensor Microwave Imager (SSM/I)
118 and the Special Sensor Microwave Imager/Sounder from August 1987 to December 2010.
119 The JRA sea ice data for the Arctic Ocean before the satellite era from January 1870 to
120 November 1978 was taken from Walsh and Chapman (2001), which used various regional
121 datasets based primarily on ship reports and aerial reconnaissance. To explore the impact of
122 the MPT on tropical cyclones, we also analyze the tropical cyclone data sets from the Joint
123 Typhoon Warning Center (JTWC) and the Tropical Prediction Center (TPC) best track
124 reanalysis from website at <http://weather.unisys.com/hurricane/>. In this study, we examine the
125 linear relationships between the dominant modes of MPT and the tropical cyclone genesis

126 numbers over the WNP and the East Pacific (EP) during the mid-summer.

127 The atmospheric data, including geopotential height and three-dimensional velocity at
128 multiple levels, are obtained from the NCEP–NCAR Reanalysis (Kalnay et al. 1996). The
129 geopotential height and horizontal wind obtained from the ERA-Interim for 1979-present are
130 also used to compare with the NCEP-NCAR data. The Niño-3.4 index is downloaded from
131 the NOAA Environmental Systems Research Laboratory’s (ESRL) website at
132 <http://www.esrl.noaa.gov/psd/data/climateindices>. The analysis period of this study is
133 1948-2014.

134 We apply an empirical orthogonal function (EOF) analysis on the mean horizontal winds
135 to capture the dominant modes of the MPT during the mid-summer (July and August) when
136 the MPT reach the maximum intensity (see Fig. 1), with an equal area weighting at each grid
137 point by multiplying the square root of the cosine of latitudes due to the decrease in area
138 toward the pole (North et al. 1982). This vector-EOF analysis enables a more thorough
139 analysis of wind components than scalar analyses (Legler 1983). Linear regression/correlation
140 analysis is performed by regressing/correlating the anomalous atmospheric circulation,
141 precipitation, and other physical quantities on/with the principle components. This study
142 focuses on the mid-summer [i.e., July–August (JA)], and so each set of successive 2-month
143 season is considered with physical fields leading or lagging the PCs [e.g., May-June (MJ) and
144 June-July (JJ) lead the PC in JA by two months and one month, respectively, while
145 August-September (AS) lag the PC in JA by one month].

146 Considering the dominant correlation between ENSO and other variables, in most of the

147 correlation/regression analyses the ENSO signal captured by the Niño-3.4 index is removed
 148 via a simple linear regression method. It should be noted that it is impossible to remove the
 149 influence of ENSO completely by only the Niño-3.4 index (Hu et al. 2016), as ENSO signal
 150 is not always linear and stationary in time (Capotondi 2015). To investigate the interannual
 151 variations of MPT and its climate effects, we also remove the linear trend of MPT before
 152 conducting the correlation/regression analysis. We used the Student's *t*-test to assess the
 153 statistical significance of results from correlation analysis. A value of correlation above 0.33
 154 (0.24), for a 36-yr (65-yr) length of 1979–2014 (1948-2014), is used to estimate the 95%
 155 confidence level. Here the correlation (*r*) is defined as

$$156 \quad r = \frac{\sum_{i=1}^n (x_i - \bar{x})(y_i - \bar{y})}{\sqrt{\sum_{i=1}^n (x_i - \bar{x})^2} \sqrt{\sum_{i=1}^n (y_i - \bar{y})^2}},$$

157 in which \bar{x} and \bar{y} are the sample mean of x_i and y_i from $i=1$ to $i=n$ (n is the sample size,
 158 and $n-2$ is the so called degree of freedom). The threshold of correlation coefficient $|r_0|$ for the
 159 95% confidence level is defined as: $|r_0| = \frac{t}{\sqrt{t^2 + (n-2)}}$, where t can be acquired by checking
 160 tables about the critical values of Student's *t* distribution with $n-2$ degrees of freedom (Storch
 161 and Zwiers 2002).

162 3. Climatological and interannual features of MPT

163 Figure 1 shows the monthly climatological patterns of 200-hPa geopotential height
 164 (H200) and its departures from the annual mean for all 12 months. Within the annual cycle,
 165 the largest changes occur over East Asia and the North Pacific, accompanied by a shift in the

166 phase of planetary-scale stationary waves. In winter (from December to February), distinct
167 trough and ridge are seen over East Asia and the west of North America, respectively, due to
168 strong land-ocean thermal contrast (Smagorinsky 1953; Wang and Ting 1999). From late
169 spring to early summer (May and June), the atmospheric circulations undergo a dramatic
170 change when the East Asian trough and the Alaskan ridge weaken rapidly, while the Asian
171 summer monsoon and the SAH are quickly established (Yeh et al. 1959; Webster and Yang
172 1992). In northern mid-summer (July and August), the SAH, the MPT, and the North
173 American ridge dominate the northern subtropics, due mainly to monsoon heating (Wang and
174 Ting, 1999). In particular, the SAH and the MPT evolve approximately in tandem, and both
175 reach their maximum intensities in July and August. After September, the SAH and the MPT
176 weakens quickly and winter patterns appear again.

177 Figure 2 shows more details about the climatological characteristics of MPT and its
178 surrounding atmospheric circulation in mid-summer (JA), when the MPT reaches the peak
179 intensity. As seen in Fig. 2a, the upper-level SAH and MPT are corresponding to the
180 lower-level Asian monsoon low and WNPSH, respectively, implying that the atmospheric
181 circulations in the northern subtropics are completely out of phase in the vertical direction.
182 Figure 2b shows the vertical cross section of zonally asymmetric height and vertical velocity
183 along 30°N. It indicates that vigorous upward motions occur under the western side of the
184 MPT due to the monsoon-related convection over East Asia and the WNP. Besides, strong
185 descending motions are found under the eastern side of the MPT, which seem to be linked to
186 the Pacific subtropical high.

187 Figure 3a shows the standardized deviations of upper-tropospheric horizontal winds, in
188 which the largest values appear over the mid-latitudes and the equatorial Pacific regions,
189 which could be attributed to the intrinsic large variability of the westerly jet streams (Joseph
190 and Sijikumar 2004; Schiemann et al. 2009) and the large variability associated with ENSO
191 (Yang and Hoskins 2013; Kim et al. 2014). There is, however, substantial variability over the
192 subtropical Pacific, coinciding with the MPT area. Overall, one expects the subtropics to be
193 stable with small variability due to the relatively weaker coupling between the upper
194 troposphere and the low troposphere (Charney 1963). Thus, it is interesting to explore why
195 large variability exists in the MPT region and whether such variability is forced locally or
196 remotely?

197 Figure 3b further shows the frequency distribution of MPT centers during the period of
198 1948-2014. The MPT centers are identified as the locations of minimum zonally-asymmetric
199 geopotential height at 200 hPa. In general, the MPT centers are distributed along a
200 northeast-southwest direction, concentrating around 30°N of latitude, with a maximum
201 frequency of 9 years located at 152.5°W and 32.5°N. In extreme cases, MPT centers can shift
202 as far northeast as to 130°W and 40°N. It can also be seen that the MPT centers tend to shift
203 more frequently in east-west direction than in south-north direction.

204 **4. Dominant modes of MPT and associated circulation anomalies**

205 *a. Vector-EOF modes of MPT variability*

206 To better classify MPT variability, an area-weighted vector-EOF analysis is applied to
207 the 200-hPa horizontal winds. The analysis domain is 160°E-120°W and 15°N-50°N, as

208 outlined by the blue box in Fig. 3a, covering the area of both maximum subtropical variability
209 and climatic position of the MPT. The first two modes respectively explain 20.4 and 13.1
210 percent of the total variance (26.5% and 14.7% for the ERA-Interim data set, 1979-2014),
211 which are statistically distinguishable from the rest of the eigenvectors according to the rule
212 by North et al. (1982).

213 The spatial patterns of the first two modes of MPT are presented in Figs. 4a and 4c, in
214 terms of the correlation coefficients between H200 and the principal components (PC1 and
215 PC2). The first mode is dominated by significant anomalies in the southwestern side of the
216 MPT (Fig. 4a), which reflects a change in MPT intensity over the WNP. The second mode,
217 however, is related with the significant anomalies in the northeastern side of the MPT (Fig.
218 4c), and it reflects the change in MPT intensity over the eastern North Pacific. The
219 corresponding time series of the two modes are illustrated in Figs. 4b and 4d. The first mode
220 exhibits strong interannual signals, combined with multi-decadal variations with a shift from
221 a predominantly negative phase to a positive phase around the 1990s. On the other hand, the
222 second mode shows a significant decreasing trend for the period of 1948-2014. The time
223 series calculated from the ERA-Interim data set are also included in Figs. 4b and 4d, which
224 are consistent with those from the NCEP-NCAR product.

225 We also repeat the vector-EOF analysis to a larger domain covering most of the
226 Northern Hemisphere (20°E-60°W, 20°N-80°N). The spatial patterns related to the first mode
227 of MPT is very similar to those patterns from the analysis of the smaller domain (with a
228 correlation coefficient of 0.77 between the two corresponding PC1), although the variance

229 explained drops to 10.5%. The previous second mode of MPT variability falls to the third
230 mode for the extended domain (with a correlation coefficient of 0.52 between the the
231 corresponding PC2). These results further demonstrate the robustness of the first two modes
232 of MPT.

233 *b. Atmospheric circulation anomalies associated with the dominant modes of MPT*

234 Figure 5 shows the regressions of atmospheric circulation and Plumb wave activity
235 fluxes (WAF; Plumb 1985) onto the dominant modes of MPT, in which the linear trends of
236 the PCs and the field variables have been subtracted. The first mode corresponds to higher
237 pressure across the entire mid-latitude belts (Fig. 5a), covering North Africa, South and East
238 Asia, the North Pacific, North America, and the Atlantic. Several isolated positive centers are
239 identified along the entire mid-latitude belts, with most prominent anomalies over the East
240 Asia, North Pacific, North America, and the North Atlantic. Meanwhile, remarkable
241 anomalies of alternative cyclonic and anti-cyclonic circulations are seen over the western
242 North Pacific. In comparison, the second mode of MPT reveals predominant signals over the
243 eastern North Pacific (Fig. 5b), which are oriented in a north-south direction, connecting the
244 tropics and the Arctic region.

245 Figures 5a and 5b show the association of WAFs with the dominant modes of MPT. The
246 first mode is associated with southward and eastward propagating wave trains, which diverge
247 over East Asia and converge in the southwestern portion of the MPT, resulting in
248 intensification of the trough at its first mode. Similarly, the second mode is related with an
249 equatorward propagating wave train, which originates from the northeastern Pacific and

250 converges in the northeastern portion of MPT, leading to strengthening of the MPT at its
251 second mode. Besides, the second mode of MPT also corresponds to a relatively weak wave
252 train originating from the central Pacific, which could be related to the central Pacific
253 warming that is shown in Fig. 6b. The anomalous WAFs seem to appear at the exit of East
254 Asian westerly jet, which may be related to the meridional displacements and the changes in
255 intensity of the jet stream. As seen in Figs. 5c-5d, an intensified MPT in the first mode is
256 significantly related to the northward shift of the jet stream over East Asia and the western
257 North Pacific, while the intensified MPT in the second mode corresponds to the weakening
258 jet stream over the eastern North Pacific. These results suggest that the wave trains associated
259 with MPT variability may be sensitive to the subtle westerly jet structure. Thus, we have also
260 computed the WAF proposed by Takaya and Nakamura (2001, TN01) to understand the
261 impact of uneven basic flow. The regressed patterns of TN01 WAFs reveals a similar pattern
262 as the Plumb's WAF (figure not shown), showing two splitting wave trains over the western
263 (first mode) and the eastern (second mode) North Pacific. One propagates eastward along the
264 westerly jet stream, and the other propagates southeastward that affects the variability of MPT.
265 Compared to the Plumb's WAFs, the equatorward propagating wave trains of TN01 WAFs
266 associated with the MPT seem to be more prominent, implying the possible effect of
267 zonally-asymmetric westerlies on MPT variability.

268 The variabilities of MPT seem to largely originate in extratropical regions. Indeed, when
269 ENSO signals were removed (figure not shown), the features of regression patterns remained
270 almost unchanged. For the first mode, the negative height anomalies over the WNP and

271 sub-Arctic regions experience a slight decrease, and the positive height anomalies over the
272 mid-latitudes remain the same and even become somehow stronger, particularly over North
273 America and the Atlantic. For the second mode, the negative height anomalies over the Arctic
274 region become even more significant. These results imply that the dominant modes of MPT
275 variability may be also affected by other forcing sources beyond ENSO.

276 The regressions of SST anomalies (SSTAs) on PCs of MPT are shown in Fig. 6. Both
277 modes are significantly correlated with the Pacific SST. The first mode is significantly related
278 with a La Niña-like pattern, with negative SSTA in the central-eastern Pacific. This mode also
279 exhibits a close relationship with the Atlantic SST. The correlation coefficient between PC1
280 (PC2) and the Niño-3.4 index is -0.465 (0.23), which exceeds the 99% (90%) confidence
281 level, implying that both the first and second modes of MPT are affected by ENSO, to
282 different a certain extent. It should also be noted that the regressed SST patterns in Figs. 6a
283 and 6b seem to represent the eastern-Pacific (EP) type and the central-Pacific (CP) type of El
284 Niño (e.g., Ashok et al. 2007; Kug et al. 2009), respectively. The EP type of El Niño
285 corresponds to northward propagating waves and anomalous high pressure on the
286 southwestern portion of MPT (Wang and Wu 2016), implying the weakening of MPT at its
287 first mode. However, the CP type of El Niño is correlated with northeastward propagating
288 waves (Fig. 5b), which lead to anomalous low pressure on the northeast portion of MPT,
289 suggesting the intensification of MPT at its second mode. Zhang et al. (2012) have
290 investigated the differences in atmospheric teleconnections associated with different types of
291 El Niño, indicating that the EP type of El Niño was associated with wave trains that tilted

292 more in north-south direction, while the CP type of El Niño was significantly correlated with
293 wave trains that tilted more in northeast-southwest direction. Their results, though focused on
294 the boreal autumn, were similar to the features shown in Figs. 5a and 5b.

295 **5. Factors and physical mechanisms for the dominant modes of MPT**

296 The maps of lead-lag correlation between global SST and PC1 (also PC2) are shown in
297 Fig. 7, where the linear signal of ENSO is removed by regressing out the Niño-3.4 index from
298 the PCs. The left panels of Fig. 7 indicate that the first mode of MPT is significantly
299 correlated with SSTAs in the equatorial and North Atlantic regions at all lags. In particular,
300 the Atlantic SSTs significantly lead the first mode by more than 4 months. This result implies
301 that the Atlantic SST may be a driver to the variations of the first mode of MPT. In the North
302 Pacific (NP), positive SSTAs are found in the simultaneous correlation. Although the NP
303 SSTAs may also contribute to the variability of MPT by altering the NP storm tracks and
304 triggering planetary waves, we tend to recognize the North Pacific SSTAs as a response to the
305 atmospheric, rather than a cause, because the NP SSTAs associated with the PCs seem to only
306 appear and strengthen during the periods when SST lags MPT.

307 Moreover, there are significant warmings in the northern Indian Ocean (NIO) and the
308 western Pacific (WP), which tend to lead the MPT by as long as 4 months, evolving gradually
309 from the NIO-WP to the North Pacific. Xie et al. (2009) indicated that the NIO-WP warming
310 could persist through the boreal summer by initiating a series of air-sea interaction, which
311 may also be a source of the North Pacific variability. Indeed, the WP warming is significantly
312 correlated to the so-called Pacific-Japan teleconnection during the boreal summer (e.g., Nitta

313 1987; Kosaka and Nakamura 2006), which bridges the climate between the Indo-Pacific and
314 North Pacific regions. However, the current study is mainly focused on the Atlantic SST
315 emphasizing its relatively robust signals in intensity and locations.

316 As seen from the right panels of Fig. 7, the second mode of MPT is only weakly
317 correlated with global SST, except for the North Pacific and Indian Ocean SSTs. It should be
318 mentioned that the Indian Ocean SSTA may be related to the residual signals of El Niño (see
319 Fig. 6b) as it is impossible to remove the non-linear effect of ENSO completely by a
320 regressed method. Significant signals are mainly observed in the correlations when the MPT
321 leads the North Pacific SST, implying that the North Pacific SSTA is a response, rather than
322 causes, to the atmosphere. What factors may be responsible for the second mode of MPT?
323 There are several reasons for exploring the possible impact of the Arctic sea ice. First, it has
324 been shown in Fig. 5b that the geopotential height anomalies associated with the second MPT
325 mode are strongly linked to Arctic signals and an equatorward wave train. Secondly, the
326 decreasing trend in PC2 is a reminiscent of the recent rapid loss of the Arctic sea ice during
327 the boreal summer (Stroeve et al. 2007; Comiso et al. 2008). These reasons lead us to
328 investigate the relationship between the MPT and the Arctic sea ice.

329 Figure 8 presents the lead-lag correlations between the second mode of MPT and the
330 Arctic sea ice concentration. When the sea ice leads the second mode by 2 months, positive
331 correlations are observed near the Bering Strait. The correlation patterns become more
332 significant and more extensive when the sea ice leads the MPT by 1 and 0 months. It should
333 be noted that both ENSO signals and linear trends have been removed from the PC2,

334 implying that the Arctic sea ice near the Bering Strait play a role in affecting the second mode
335 of MPT.

336 Figure 9 shows the lead-lag regression maps of H200 and WAF onto the first two modes
337 of MPT. For the first mode of MPT, significant anomalies of H200 occur over the North
338 Atlantic, North Africa, and the Eurasian continent during the period when the physical fields
339 lead the MPT by 2-3 months. By the period of one-month lead, anomalous high pressures
340 emerge over the North Pacific and strengthen substantially in JA and AS, which are
341 accompanied by enhanced WAFs. In comparison, significant anomalies of H200 associated
342 with the second mode of MPT mainly appear over the Arctic regions, leading the PC2 by 2
343 months, which subsequently induce an equatorward wave train over the eastern North Pacific
344 in JJ and JA. That is, although significantly antecedent signals associated with the MPT can
345 be found over the Atlantic and Arctic regions, the anomalous wave trains that affect the MPT
346 emerge only one-month in advance, implying that the seasonally-varying basic flow
347 influences the triggering of anomalous wave trains related to the MPT. Moreover, the
348 intensification of the anomalies over the western/eastern North Pacific suggests an interaction
349 between the Atlantic/Arctic forced signals and the Pacific jet stream variability, or the internal
350 atmospheric dynamics that plays an important role.

351 To better explain how the Atlantic SST and the Arctic sea ice influence the MPT, we
352 define two indices from the domain-averaged values: the Atlantic SST (ASST), calculated as
353 $ASST = SST(A) + SST(B)$, where A and B represent the regions outlined by the black boxes
354 in Fig. 7 and the Arctic sea ice concentration (ASIC), calculated as $ASIC = ASIC(C)$, where

355 C denotes the region near the Bering Strait outlined in Fig. 8. The selections of boxes A, B,
356 and C are based on the lag-lead correlation relationships between the Atlantic SST / Arctic SIC
357 and the PCs. We have tested with different regions such as the entire North Atlantic
358 (80°W - 10°W , 0 - 55°N) and obtained similar results (not shown).

359 Figures 10a and 10b show the ASST and ASIC indices. As seen in Fig. 10a, except for
360 the warming trends, the ASST also shows profound interannual and multi-decadal variations,
361 switching from a predominant negative phase to a positive phase around the mid-1990s. The
362 correlation coefficient between ASST (de-trend) and the PC1 is 0.41, exceeding the 95%
363 confidence level. Figures 10(c) and 10(d) show the regression maps of H200 and WAF onto
364 the de-trended ASST and the interannual component of ASST (by subtracting the 9-year low
365 filtering of de-trend ASST), respectively. Although significant anomalies of H200 associated
366 with the de-trend ASST can be observed within the MPT domain (Fig. 10c), the physical
367 mechanism is unclear due to the ambiguity of teleconnection pattern. In comparison, after
368 removing the low-frequency component of ASST, an anomalous wave train is clearly seen over
369 the Eurasian continent (Fig. 10d), which originates from the North Atlantic and eventually
370 affects the southwestern portion of MPT. On the other hand, except for a sharply decreasing
371 trend, the Arctic sea ice also shows considerable interannual variability. The correlation
372 coefficient between ASIC (de-trend) and the PC2 is 0.36, which exceeds the 95% confidence
373 level. As seen in Fig. 10e, the ASIC shows significant correlations with H200 and WAF over
374 the eastern North Pacific. Positive Arctic sea ice anomaly can lower tropospheric geopotential
375 height over the Arctic regions due to surface cooling, which subsequently induces an

376 equatorward propagating wave train that deepens the MPT on its northeastern portion.

377 **6. Associated Asian-Pacific-North American climate anomalies**

378 *a. Precipitation and surface air temperature*

379 Figure 11 shows the correlation of Asian and North American precipitations with the
380 PCs of MPT, in which the linear trends have been removed from the PCs. As shown in Figs.
381 11a-11b, more precipitation over South Asia, northern China, and eastern U.S. and less
382 precipitation over the Yangtze Basin, southern Japan, and northern U.S. are associated with
383 the first mode of MPT. The features associated with the second mode are quite different.
384 Figures 11c-11d show that correlations are dispersed and less significant over South Asia, and
385 that precipitation is significantly light over southwestern U.S. in association with the second
386 mode.

387 When ENSO signals are removed, the correlations between Asian precipitation and the
388 PCs decrease substantially, especially over South Asia (figure not shown). Nevertheless, the
389 correlation patterns over North America suffer little change. If the ASST (ASIC) signals are
390 removed, however, the patterns of correlation with the PCs become insignificant over North
391 America, but remain similar with the previous over South Asia, implying the important roles
392 of the Atlantic SST and the Arctic sea ice. It is also possible that both precipitation and MPT
393 patterns may respond to ENSO separately and the link between MPT and the precipitation
394 over South and East Asia may be weak.

395 The relationships between surface air temperature (SAT) and the dominant modes of
396 MPT are shown in Fig. 12. Corresponding to the first mode (Figs. 12a-12b), warmer SAT

397 occurs across almost the entire middle latitudes, including the Middle East, East Asia, and
398 northern U.S. Over South Asia, colder SAT is seen with a relation to more precipitation.
399 Associated with the second mode, significantly warmer SAT appears over southwestern U.S.,
400 which coincides well with less precipitation over the region. Our analysis reveals a feature
401 (figure not shown) that is identical to the previous: the patterns of correlation between Asian
402 (North American) SAT and the PCs of MPT are strongly modulated by ENSO (Atlantic
403 SSTAs and Arctic sea ice). Indeed, the anomalous atmospheric circulations related to the
404 dominant modes of MPT show a barotropic structure. Under the control of high pressures,
405 enhanced descending motions suppress convection and allow more incoming radiation, which
406 results in less precipitation and warmer surface air temperature, and vice versa.

407 *b. WNP and EP tropical cyclones*

408 Climatologically, the MPT is associated with strong ascending and descending motions
409 under its upstream and downstream portions (Fig. 2b), respectively. Figure 13 shows the
410 correlations between outgoing longwave radiation and the first two PCs of the trough, where
411 both ENSO signals and linear trends have been removed from the PCs based on the
412 ERA-Interim data. An intensified MPT in the first mode is significantly correlated with
413 enhanced convection over the WNP and suppressed convection over the CP. However, an
414 intensified MPT in the second mode corresponds to stronger convection over the WP and the
415 northeastern Pacific, accompanied with suppressed convection over the EP and Central
416 America. Therefore, for both the modes, an intensified MPT tends to contribute upward
417 motions over the WNP/WP and descending motions over the CP/EP, which affect the

418 occurrence of WNP and EP TCs, given that the WNP TCs and the EP TCs mainly occur and
419 develop beneath the upstream and downstream portions of the MPT, respectively.

420 Figure 14 shows the scatter diagrams of the TC genesis numbers over the WNP/EP and
421 the PCs. It should be noted that the TC samples used in these figures only include the TCs for
422 the period of 1979-2014 due to the relatively weaker relationship between the MPT and the
423 TC genesis numbers for the earlier period, which could be related to the relatively poor data
424 quality before 1979. Again, both ENSO signals and linear trends in the PCs have been
425 excluded. As seen in Fig. 14a, an intensified MPT in the first mode tends to increase the WNP
426 TC numbers, but their correlation is insignificant, with a coefficient of 0.17. However, the
427 first mode of MPT presents a much stronger relationship with the EP TC numbers and tends
428 to decrease the EP TC numbers (Fig. 14c), with a correlation coefficient of -0.311.

429 In comparison, the second mode of MPT shows stronger relationships with the TC
430 numbers over both WNP and EP. Figures 14b and 14d indicate that a strengthened MPT in
431 the second mode favors generation of the WNP TCs but suppresses the occurrences of the EP
432 TCs. The coefficient of correlation between the WNP (EP) TC numbers and the PC2 is 0.45
433 (-0.33), statistically exceeding the 99% (95%) confidence level with an effective degree of
434 freedom of 33 for a total of 35 seasons (1979–2014).

435 Therefore, for both the first mode and the second mode, an intensification of the MPT is
436 associated with more TCs over the WNP but less TCs over the EP. As shown in Fig. 13, an
437 intensified MPT compels stronger upward (downward) motions in its upstream (downstream)
438 portion, providing favorable (unfavorable) conditions for TC genesis over the WNP (EP). The

439 relationships of the two MPT modes with WNP/EP TCs are different in several aspects. The
440 first mode is more strongly connected with the EP TCs, compared with the WNP TCs.
441 However, the second mode shows a more robust relationship with the WNP TCs than with the
442 EP TCs. These features should be related to the large-scale circulation conditions that are
443 induced by the MPT.

444 **7. Summary and discussion**

445 This paper has documented the climatological and interannual characteristics of the MPT
446 including the dominant modes of the trough and their associated climate anomalies. The MPT
447 acts as an atmospheric bridge that connects the climate over Asia and North America, with
448 strong ascending (descending) motions on its western (eastern) side. Climatologically, the
449 MPT peaks at the 200-hPa and 150-hPa levels during mid-summer and extends from the
450 mid-latitudes to the subtropics in a southwest-northeast direction. It varies in tandem with the
451 SAH.

452 The MPT exhibits a large interannual variability. Its first (second) mode reflects a
453 change in the intensity of the trough on its southwestern (northeastern) side. Both modes of
454 the MPT are significantly correlated with the tropical Pacific SST. Moreover, the first MPT
455 mode is significantly correlated to the Atlantic SST, and the second MPT mode is linked with
456 the variation of Arctic sea ice near the Bering Strait. On the one hand, the Atlantic warming
457 would increase the upper-level geopotential height, which triggers an eastward propagating
458 wave train across the Eurasian continent, and intensifies the MPT on its southwestern portion.
459 On the other hand, a positive Arctic sea ice anomaly can lower the upper tropospheric

460 geopotential height near the Bering Strait due to surface cooling, which induces an
461 equatorward propagating wave train that deepens the MPT on its northeastern portion.

462 Associated with an intensification of the MPT on its southwestern side, more (less)
463 precipitation occurs over South Asia and northern China (the Yangtze-River basin and South
464 Japan). Correspondingly, warmer (colder) SAT appears over East Asia (South Asia) due to
465 the control of an anomalous high pressure (monsoon convection). However, the second mode
466 of MPT shows sporadic and less significant relationships with Asian precipitation and SAT.
467 The relationship between Asian climate and the MPT is strongly modulated by ENSO. When
468 ENSO signals are removed, the patterns of correlation between the trough and Asian
469 precipitation/SAT over South Asia and East Asia change remarkably.

470 The first (second) mode of MPT is also significantly related with the precipitation and
471 SAT over northern (southwestern) U.S., attributed mainly to the Atlantic SST (the Arctic sea
472 ice near the Bering Strait). The patterns of correlation between the MPT and North American
473 climate suffer little influence from ENSO, but are strongly affected by the Atlantic SST and
474 the Arctic sea ice near the Bering Strait.

475 The numbers of tropical cyclone genesis over the WNP and the EP are also closely
476 related to the dominant modes of MPT. Both the first mode and the second mode of MPT are
477 positively (negatively) correlated with the TC numbers over WNP (EP). An intensified MPT
478 is accompanied by more TCs over the WNP and less TCs over the EP. However, the first
479 (second) mode of MPT presents a stronger relationship with the TC numbers over EP (WNP),
480 compared to WNP (EP). Overall, the second mode of MPT is more strongly connected with

481 the WNP and EP TC numbers than the first mode.

482 It should be pointed out that although we have presented the relationship between the
483 dominant modes of MPT and the numbers of Pacific tropical cyclones, the cause-and-effect
484 aspect of this relationship deserves more investigations. The tropical cyclones may also
485 influence the MPT through Rossby wave energy dispersion associated with the TCs (Ferreira
486 and Schubert 1999). However, considering the relative spatial and time scales between the
487 MPT and the TCs, it is more likely that the MPT modulates the TC genesis (Hu et al. 2017).
488 In addition, although the dominant modes of MPT are significantly related to the Pacific and
489 Atlantic SSTs and the Arctic sea ice, the impact from the atmospheric intrinsic variability,
490 such as the circumglobal teleconnection, should not be excluded.

491

492 **Acknowledgments.** The authors wish to thank Profs. Ming Cai, Zhaohua Wu, and Jianhua Lu
493 for a number of constructive discussions. The comments from three anonymous reviewers are
494 helpful for improving the overall quality of this paper. This study was supported by the
495 National Key Research and Development Program of China (2016YFA0602703), the
496 National Key Scientific Research Plan of China (Grant 2014CB953900), the National Natural
497 Science Foundation of China (Grants 41690123, 41690120, 91637208, and 41661144019),
498 and the CMA Guangzhou Joint Research Center for Atmospheric Sciences.

499

500

501

502 **REFERENCES**

- 503 Ashok, K., S. K. Behera, S. A. Rao, H. Weng, and T. Yamagata, 2007: El Niño Modoki and its
504 possible teleconnection. *J. Geophys. Res.*, **112**, C11007.
- 505 Capotondi A., 2015: Atmospheric science: Extreme La Nina events to increase. *Nature*
506 *Climate Change*, **5**, 100–101.
- 507 Charney, J. G., 1963: A note on large-scale motions in the tropics. *J. Atmos. Sci.*, **20**, 607–609.
- 508 Colton, D. E., 1973: Barotropic scale interactions in the tropical upper troposphere during the
509 northern summer. *J. Atmos. Sci.*, **30**, 1287–1302.
- 510 Comiso, J. C., C. L. Parkinson, R. Gersten, and L. Stock, 2008: Accelerated decline in the
511 Arctic sea ice cover. *Geophys. Res. Lett.*, **35**, L01703.
- 512 Ding, Q., and B. Wang, 2007: Intraseasonal teleconnection between the summer Eurasian
513 wave train and the Indian monsoon. *J. Climate*, **20**, 3751–3767.
- 514 Ferreira, R. N., and W. H. Schubert, 1999: The role of tropical cyclones in the formation of
515 tropical upper-tropospheric troughs. *J. Atmos. Sci.*, **56**, 2891–2907.
- 516 Gray, W. M., 1968: Global view of the origin of tropical disturbances and storms. *Mon. Wea.*
517 *Rev.*, **96**, 669–700.
- 518 Hirahara, S., M. Ishii, and Y. Fukuda, 2014: Centennial-scale sea surface temperature analysis
519 and its uncertainty. *J. Climate*, **27**, 57–75.
- 520 Hu, C., Q. Wu, S. Yang, Y. Yao, D. Chan, Z. Li, and K. Deng, 2016: A Linkage Observed
521 between Austral Autumn Antarctic Oscillation and Preceding Southern Ocean SST
522 Anomalies. *J. Climate*, **29**, 2109–2122.

523 Hu, C., C. Zhang, S. Yang, and D. Chen, 2017: Northwestward shift of tropical cyclogenesis
524 locations over the western North Pacific modulated by ENSO and the 1998 Pacific
525 climate regime shift. Submitted to *Climate Dynamics*.

526 Hodanish, S., and W. M. Gray, 1993: An observational analysis of tropical cyclone
527 recurvature. *Mon Wea. Rev.*, **121**, 2665–2689.

528 Hoskins, B. J., and M. J. Rodwell, 1995: A model of the Asian summer monsoon. Part I: The
529 global scale. *J. Atmos. Sci.*, **52**, 1329–1340.

530 Huang, B., V. F. Banzon, E. Freeman, J. Lawrimore, W. Liu, T. C. Peterson, T. M. Smith, P. W.
531 Thorne, S. D. Woodruff, and H.-M. Zhang, 2015: Extended reconstructed sea surface
532 temperature version 4 (ERSST.v4). Part I: Upgrades and intercomparisons. *J. Climate*,
533 **28**, 911–930.

534 Joseph, P. V., and S. Sijikumar, 2004: Intraseasonal variability of the low-level jet stream of
535 the Asian summer monsoon. *J. Climate*, **17**, 1449–1458.

536 Kalnay, E., M. Kanamitsu, R. Kistler, W. Collins, D. Deaven, L. Gandin, M. Iredell, S. Saha,
537 G. White, J. Woollen, Y. Zhu, A. Leetmaa, R. Reynolds, M. Chelliah, W. Ebisuzaki, W.
538 Higgins, J. Janowiak, K. C. Mo, C. Ropelewski, J. Wang, Roy Jenne, and Dennis Joseph,
539 1996: The NCEP/NCAR 40-year reanalysis project. *Bull. Amer. Meteor. Soc.*, **77**, 437–
540 471.

541 Kelly, W. E., and D. R. Mock, 1982: A diagnostic study of upper tropospheric cold lows over
542 the western North Pacific. *Mon. Wea. Rev.*, **110**, 471–480.

543 Kim, S.-T., W. Cai, F.-F. Jin, and J.-Y. Yu, 2014: ENSO stability in coupled climate models

544 and its association with mean state. *Climate Dyn.*, **42**, 3313–3321.

545 Kosaka, Y., and H. Nakamura, 2006: Structure and dynamics of the summertime
546 Pacific-Japan teleconnection pattern. *Quart. J. Roy. Meteor. Soc.*, **132**, 2009–2030.

547 Kousky, V., and M. A. Gan, 1981: Upper tropospheric cyclonic vortices in the tropical South
548 Atlantic. *Tellus*, **33**, 538–551.

549 Krishnamurti, T. N., 1971: Observational study of the tropical upper tropospheric motion field
550 during the northern hemisphere summer. *J. Appl. Meteor.*, **10**, 1066–1096.

551 Kug, J.-S., F.-F. Jin, and S.-I. An, 2009: Two types of El Niño events: Cold tongue El Niño
552 and warm pool El Niño. *J. Climate*, **22**, 1499–1515.

553 Legler, D. M., 1983: Empirical orthogonal function analysis of wind vectors over the tropical
554 Pacific region. *Bull. Amer. Meteor. Soc.*, **64**, 234–241.

555 Magaña, V., and M. Yanai, 1991: Tropical-midlatitude interaction on the time scale of 30 to
556 60 days during the northern summer of 1979. *J. Climate*, **4**, 180–201.

557 Montgomery, M. T., and B. F. Farrell, 1993: Tropical cyclone formation. *J. Atmos. Sci.*, **50**,
558 285–310.

559 Nitta, T., 1987: Convective activities in the tropical western Pacific and their impacts on the
560 Northern Hemisphere summer circulation. *J. Meteor. Soc. Japan*, **65**, 373–390.

561 North, G. R., T. L. Bell, R. F. Cahalan, and F. J. Moeng, 1982: Sampling errors in the
562 estimation of empirical orthogonal functions. *Mon. Wea. Rev.*, **110**, 699–706.

563 Patla, J. E., D. Stevens, and G. M. Barnes, 2009: A conceptual model for the influence of
564 MPT cells on tropical cyclone motion in the Northwest Pacific Ocean. *Wea. Forecasting*,

565 **24**, 1215–1235.

566 Pfeffer, R. L., and M. Challa, 1992: The role of environmental asymmetries in Atlantic
567 hurricane formation. *J. Atmos. Sci.*, **49**, 1051–1059.

568 Plumb, R. A., 1985: On the three-dimensional propagation of stationary waves. *J. Atmos. Sci.*,
569 **42**, 217–229.

570 Price, J. D., and G. Vaughan, 1992: Statistical studies of cut-off-low systems. *Annales*
571 *Geophysicae*, **10**, 96–102.

572 Rasmusson, E., and T. Carpenter, 1982: Variations in tropical sea surface temperature and
573 surface wind fields associated with the Southern Oscillation/El Niño. *Mon. Wea. Rev.*,
574 **110**, 354–384.

575 Ropelewski, C., and M. Halpert, 1987: Global and regional scale precipitation patterns
576 associated with the El Niño/Southern Oscillation. *Mon. Wea. Res.*, **115**, 1606-1626.

577 Sadler, J. C., 1967: The tropical upper tropospheric trough as a secondary source of typhoons
578 and a primary source of trade wind disturbances. Hawaii Institute of Geophysics, Rep.
579 No. HIG 67–12, 44 pp.

580 ———, 1976: A role of the tropical upper tropospheric trough in early season typhoon
581 development. *Mon. Wea. Rev.*, **104**, 1266–1278.

582 ———, 1978: Mid-season typhoon development and intensity changes and the tropical upper
583 tropospheric trough. *Mon. Wea. Rev.*, **106**, 1137–1152.

584 Schiemann, R., D. Lüthi, and C. Schär, 2009: Seasonality and interannual variability of the
585 westerly jet in the Tibetan Plateau region. *J. Climate*, **22**, 2940–2957.

586 Schneider, U., B. Andreas, F. Peter, M.-C. Anja, R. Bruno, and Z. Markus, 2011: GPCP full
587 data reanalysis version 6.0 at 1.0°: Monthly land-surface precipitation from rain-gauges
588 built on GTS-based and historic data. DOI: 10.5676/DWD_GPCP/FD_M_V7_100.

589 Smagorinsky, J., 1953: The dynamical influence of large-scale heat sources and sinks on the
590 quasi-stationary mean motions of the atmosphere. *Quart. J. Roy. Meteor. Soc.*, **79**, 342–
591 366.

592 Storch, H., and F. Zwiers, 2002: *Statistical Analysis in Climate Research*. Cambridge
593 University Press, pp146.

594 Stroeve, J., M. M. Holland, W. Meier, T. Scambos, and M. C. Serreze, 2007: Arctic sea ice
595 decline: Faster than forecast. *Geophys. Res. Lett.*, **34**, L09501.

596 Takaya, K., and H. Nakamura, 2001: A formulation of a phase-independent wave-activity flux
597 for stationary and migratory quasigeostrophic eddies on a zonally varying basic flow. *J.*
598 *Atmos. Sci.*, **58**, 608–627.

599 Tomas, R. A., and P. J. Webster, 1994: Horizontal and vertical structure of cross-equatorial
600 wave propagation. *J. Atmos. Sci.*, **51**, 1417–1430.

601 Walsh, J. E., and W. L. Chapman, 2001: Twentieth-century sea ice variations from
602 observational data. *Ann. Glaciol.*, **33**, 444–448.

603 Wang, C., and L. Wu, 2016: Interannual shift of the tropical upper-tropospheric trough and its
604 influence on tropical cyclone formation over the western North Pacific. *J. Climate*, **29**,
605 4203–4211.

606 Wang, H.-L., and M. Ting, 1999: Seasonal cycle of the climatological stationary waves in

607 the NCEP/NCAR reanalysis data. *J. Atmos. Sci.*, **56**, 3892–3919.

608 Waugh, D. W., and L. M. Polvani, 2000: Climatology of intrusions into the tropical upper
609 troposphere. *Geophys. Res. Lett.*, **27**, 3857–3860.

610 Webster, P. J., 1972: Response of the tropical atmosphere to local, steady forcing. *Mon. Wea.*
611 *Rev.*, **100**, 518–541.

612 ———, and J. R. Holton, 1982: Cross-equatorial response to middle-latitude forcing in a
613 zonally varying basic state. *J. Atmos. Sci.*, **39**, 722–733.

614 ———, and S. Yang, 1989: The Three-Dimensional structure of perturbation kinetic energy and
615 its relationship to the zonal wind field. *J. Climate*, **2**, 1210–1222.

616 ———, and S. Yang, 1992: Monsoon and ENSO: Selectively interactive systems. *Quart. J. Roy.*
617 *Meteor. Soc.*, **118**, 877–926.

618 Whitfield, M. B., and S. W. Lyons, 1992: An upper-tropospheric low over Texas during
619 summer. *Wea. Forecasting*, **7**, 89–106.

620 Wu, L., C. Wang, and B. Wang, 2015: Westward shift of western North Pacific tropical
621 cyclogenesis, *Geophys. Res. Lett.*, **42**, 1537–1542.

622 Xie, S.-P., K. Hu, J. Hafner, H. Tokinaga, Y. Du, G. Huang, and T. Sampe, 2009: Indian
623 Ocean capacitor effect on Indo-western Pacific climate during the summer following El
624 Niño. *J. Climate*, **22**, 730–747.

625 Yang, G.-Y., and B. Hoskins, 2013: ENSO impact on Kelvin waves and associated tropical
626 convection. *J. Atmos. Sci.*, **70**, 3513–3532

627 Yeh, T.-Z., S.-Y. Tao, and M.-T. Li, 1959: The abrupt change of circulation over the northern

628 hemisphere during June and October. *The Atmosphere and the Sea in Motion*, B. Bolin,
629 Ed., *Rockefeller Institute Press*, 249–267.

630 Zhang, P., S. Yang, and V. E. Kousky, 2005: South Asian high and Asian-Pacific-American
631 climate teleconnection. *Adv. Atmos. Sci.*, **22**, 915–923.

632 Zhang, W., F.-F. Jin, H.-L. Ren, J. Li, and J.-X. Zhao, 2012: Differences in teleconnection
633 over the North Pacific and rainfall shift over the USA associated with two types of El
634 Niño during boreal autumn. *J. Meteor. Soc. Japan*, **90**, 535–552.

635 Zhao, P., Y.-N. Zhu, and R. H. Zhang, 2007b: An Asia-Pacific teleconnection in summer
636 tropospheric temperature and associated Asian climate variability. *Climate Dyn.*, **29**,
637 293–303.

638

639

640

641

642

643

644

645

646

647

648

649

650

651

652

653

654

655

656

657

658

659

660

661

662

663 **List of Figure Captions**

664 **Figure 1.** Climatological patterns of H200 (black contours) and its corresponding departures
665 from the annual mean (shadings). Blue contours in July and August outline the locations of
666 MPT. The abbreviations for different months were drawn at the down left corner of each
667 subplot.

668 **Figure 2.** (a) Climatological patterns of atmospheric circulation at different pressure levels
669 during boreal mid-summer (July and August, JA). The blue contours and shadings show H200
670 and H500, respectively. The vectors depict 850-hPa horizontal winds (unit: m s^{-1} ; vectors less
671 than 2 m s^{-1} are omitted). (b) Zonally asymmetric geopotential height from the zonal mean
672 (shadings) and the vertical p -velocity (contours, multiplied by a factor of 100, unit: Pa s^{-1}).

673 **Figure 3.** (a) Standard deviations of 200-hPa horizontal winds (Shadings), which are overlaid
674 by climatological H200 and UV200. The blue square box outlines the domain (160°E - 120°W ,
675 15°N - 50°N), which is selected for a vector-EOF analysis that will be used in Fig. 4. (b)
676 Enlargement of the blue-box domain, illustrating the frequency distribution of MPT centers
677 and the climatological zonally asymmetric height. Each of the numbers in (b) indicates the
678 times and locations that the MPT centers repeat.

679 **Figure 4.** The left panel depicts the correlation patterns (shadings) between H200 and the first
680 two PCs, which are overlaid by the climatological H200 (contours). The normalized PC1s and
681 PC2s are plotted in (b) and (d), respectively. The green lines in (b) and (d) indicate the PCs
682 calculated from the ERA-Interim data set. The black dashed line in (d) shows a downward
683 trend in PC2, which significantly exceeds the 99% confidence level.

684 **Figure 5.** Regressions of H200 (shading, m) and Plumb wave activity fluxes (WAF, $\text{m}^2\cdot\text{s}^{-2}$)
685 on PC1 (a) and PC2 (b). (c) and (d) are similar to (a) and (b) except for U200. Areas enclosed
686 by the white contours in each plot indicate the values significantly exceeding the 95%
687 confidence level. The black contours in (c) and (d) represent the climatology of U200 in JA.

688 **Figure 6.** Regression maps of SST and 850-hPa horizontal winds on PC1 (a) and PC2 (b).
689 Areas enclosed by the white contours present the SST anomalies exceeding the 95%
690 confidence level. Wind anomalies with a significant u or v component above the 95%
691 confidence level are plotted.

692 **Figure 7.** Lag-lead correlation maps between SST and PC1/PC2 (left/right), where the ENSO
693 signals captured by the Niño-3.4 index have been eliminated from PCs. The leading or
694 lagging months are labelled in each panel (e.g., -2 and -1 mean that the physical fields lead
695 the PCs by two and one months, while +1 denotes that the physical fields lag the PCs by one
696 month). The black square boxes outline the domains ($70^\circ\text{W}-10^\circ\text{W}$, $0^\circ\text{N}-20^\circ\text{N}$; $70^\circ\text{W}-20^\circ\text{W}$,
697 $30^\circ\text{N}-55^\circ\text{N}$) that are selected to calculate the Atlantic SST index (ASST).

698 **Figure 8.** Lag-lead correlation maps between the Arctic sea ice concentration and PC2, where
699 the ENSO signals captured by the Niño-3.4 index have been eliminated from PC2. Areas
700 outlined by the enclosed lines ($130^\circ\text{E}-170^\circ\text{W}$, $70^\circ\text{N}-80^\circ\text{N}$) are used to calculate the Arctic sea
701 ice index (ASIC).

702 **Figure 9.** Lag-lead regression maps between H200 and WAF and PC1/PC2 (left/right), where
703 the ENSO signals captured by the Niño-3.4 index have been eliminated from PCs. The
704 leading or lagging months are labelled in each panel (e.g., -2 and -1 mean that the physical

705 fields lead the PCs by two and one months, while +1 denotes that the physical fields lag the
706 PCs by one month). The black square boxes indicate the climatological location of MPT.

707 **Figure 10.** Green lines in (a)–(b) show the original ASST and ASIC indices. Bars in (a) and
708 (b) indicate the residual signals after subtracting the linear trends (black lines). (c) and (e)
709 show the regression maps of H200 (contour, m) and WAF (vector, $\text{m}^2\cdot\text{s}^{-2}$) on the detrended
710 indices of ASST and ASIC, and (d) is similar as (a) except for regressions onto the
711 interannual variations (subtracting 9-year low filtering signals) of ASST. Shadings denote the
712 correlation coefficients between H200 and the corresponding indices. Shading values of
713 ± 0.22 , ± 0.26 , and ± 0.34 indicate the thresholds exceeding the 90%, 95%, and 99% confidence
714 levels for a degree of freedom of 55, respectively.

715 **Figure 11.** The upper panel shows the correlation maps between PC1 and the land
716 precipitation over Asia (a) and North America (b). The lower panel is similar to the upper
717 panel, but for the PC2. The contours values of ± 0.24 indicate the areas exceeding the 95%
718 confidence level. The linear trends have been removed from the PCs.

719 **Figure 12.** The upper panel shows the correlation maps between PC1 and the land surface
720 temperature over Asia (a) and North America (b). The lower panel is similar to the upper
721 panel, but for the PC2. The contours values of ± 0.24 indicate the areas exceeding the 95%
722 confidence level. The linear trends have been removed from the PCs.

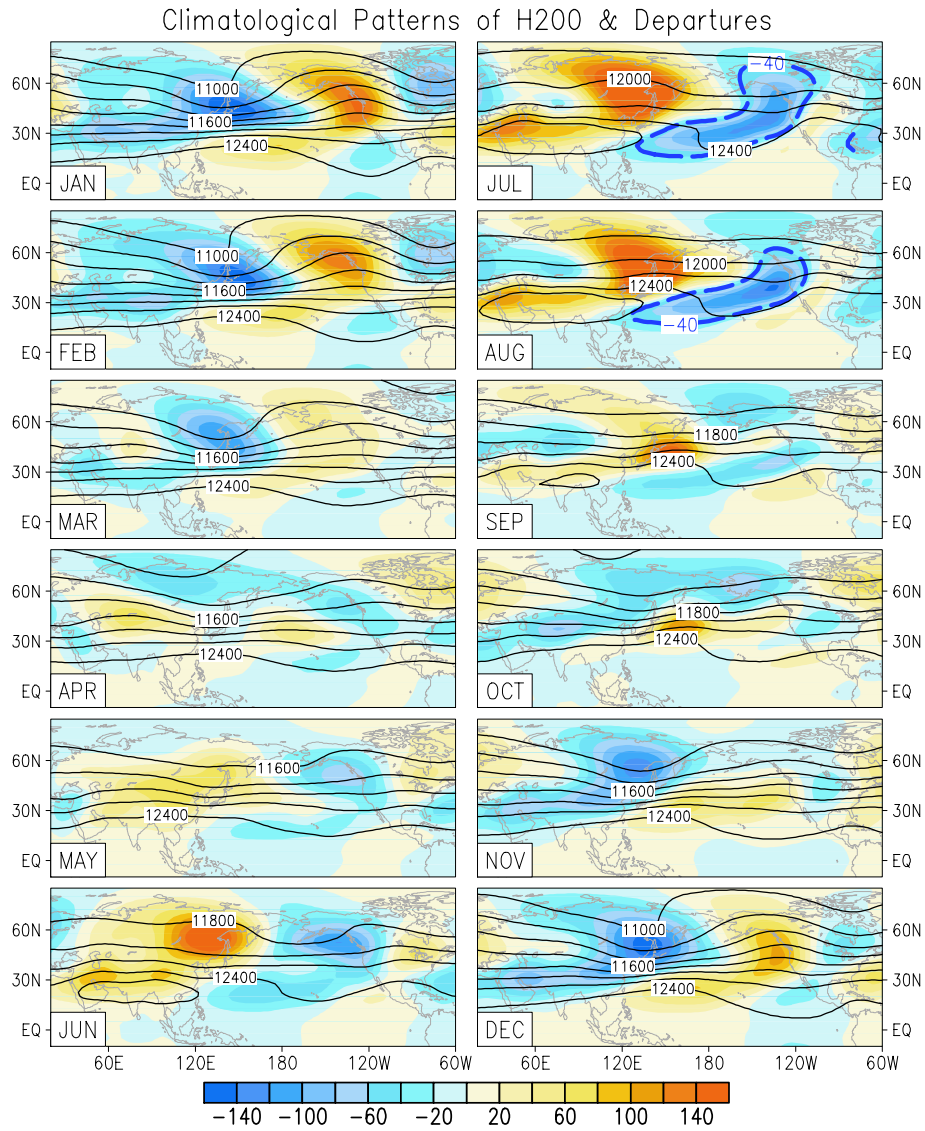
723 **Figure 13.** Correlation maps (shading) of outgoing longwave radiation (OLR) with PC1 (a)
724 and PC2 (b), where ENSO signals and linear trends have been removed from the PCs. The
725 black contours represent the climatology of H200 in JA. The green and blue markers indicate

726 the genesis positions of WNP and EP tropical cyclones during boreal summer, respectively.

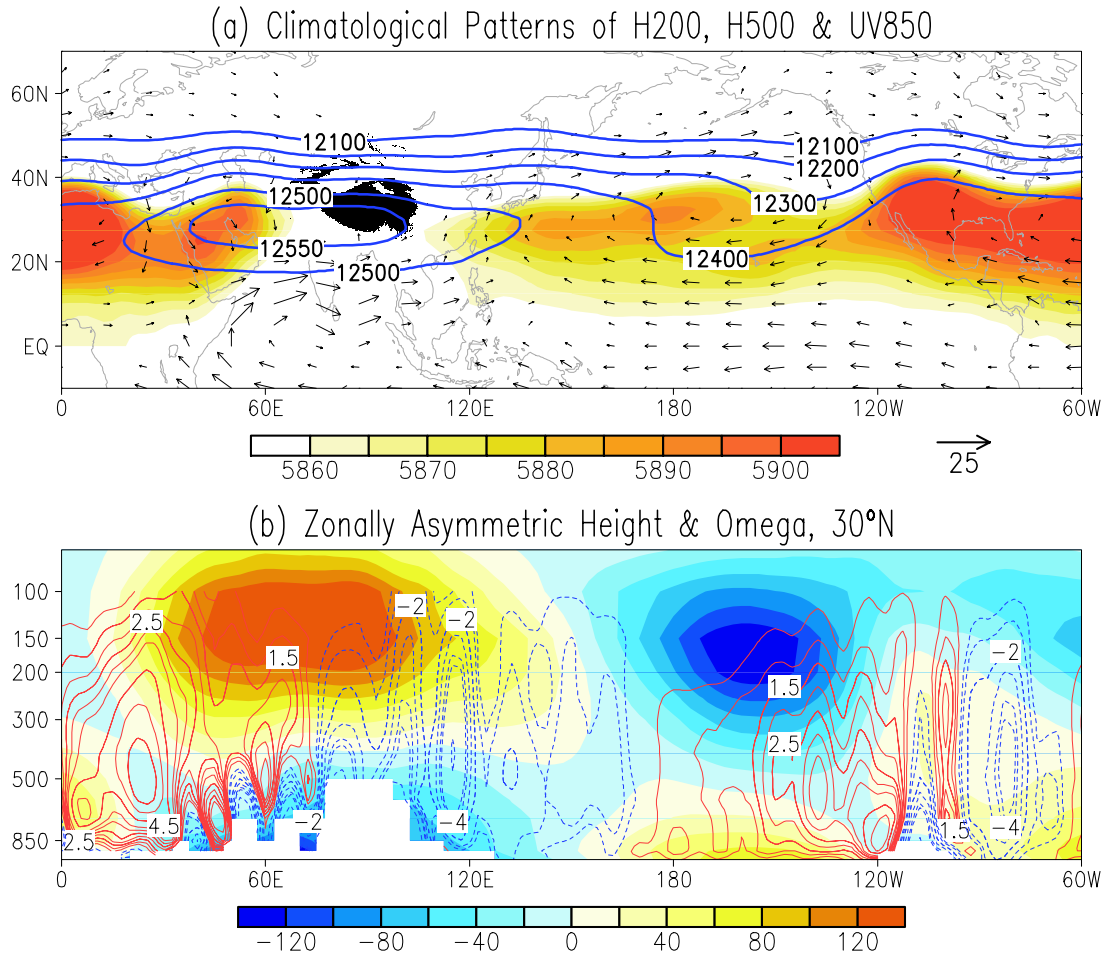
727 **Figure 14.** Scatter plots between TC genesis numbers and PCs, where both ENSO signals and
728 linear trends have been removed from the PCs. WNP and EP indicate the western North
729 Pacific and the eastern Pacific, respectively. The correlation coefficients between TC genesis
730 numbers and PCs are shown in each subplot.

731
732
733
734
735
736
737
738
739
740
741
742
743
744
745
746
747
748
749
750
751
752
753
754
755
756
757
758
759
760
761

762 **List of Figure**



765 **Figure 1.** Climatological patterns of H200 (black contours) and its corresponding departures
766 from the annual mean (shadings). Blue contours in July and August outline the locations of
767 MPT. The abbreviations for different months were drawn at the down left corner of each
768 subplot.



769

770

771 **Figure 2.** (a) Climatological patterns of atmospheric circulation at different pressure levels

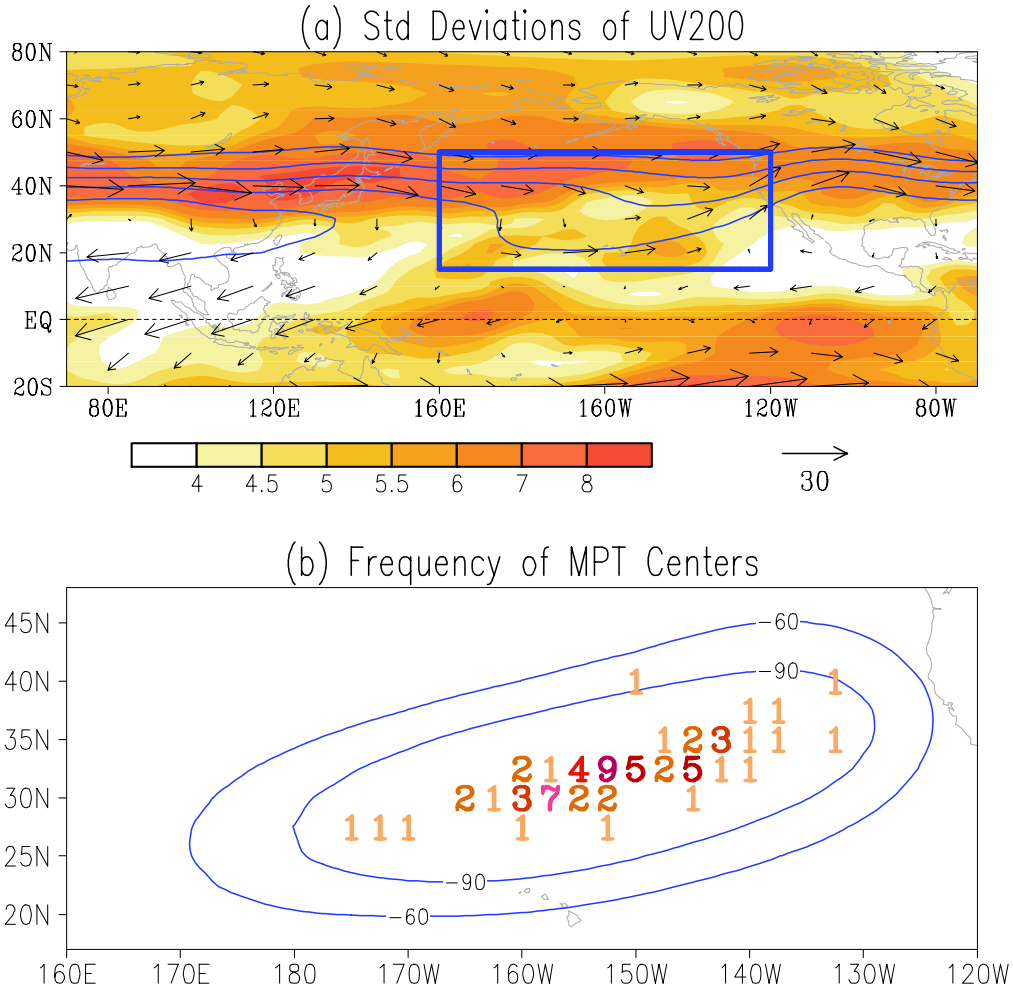
772 during boreal mid-summer (July and August, JA). The blue contours and shadings show H200

773 and H500, respectively. The vectors depict 850-hPa horizontal winds (unit: m s^{-1} ; vectors less

774 than 2 m s^{-1} are omitted). (b) Zonally asymmetric geopotential height from the zonal mean

775 (shadings) and the vertical p -velocity (contours, multiplied by a factor of 100, unit: Pa s^{-1}).

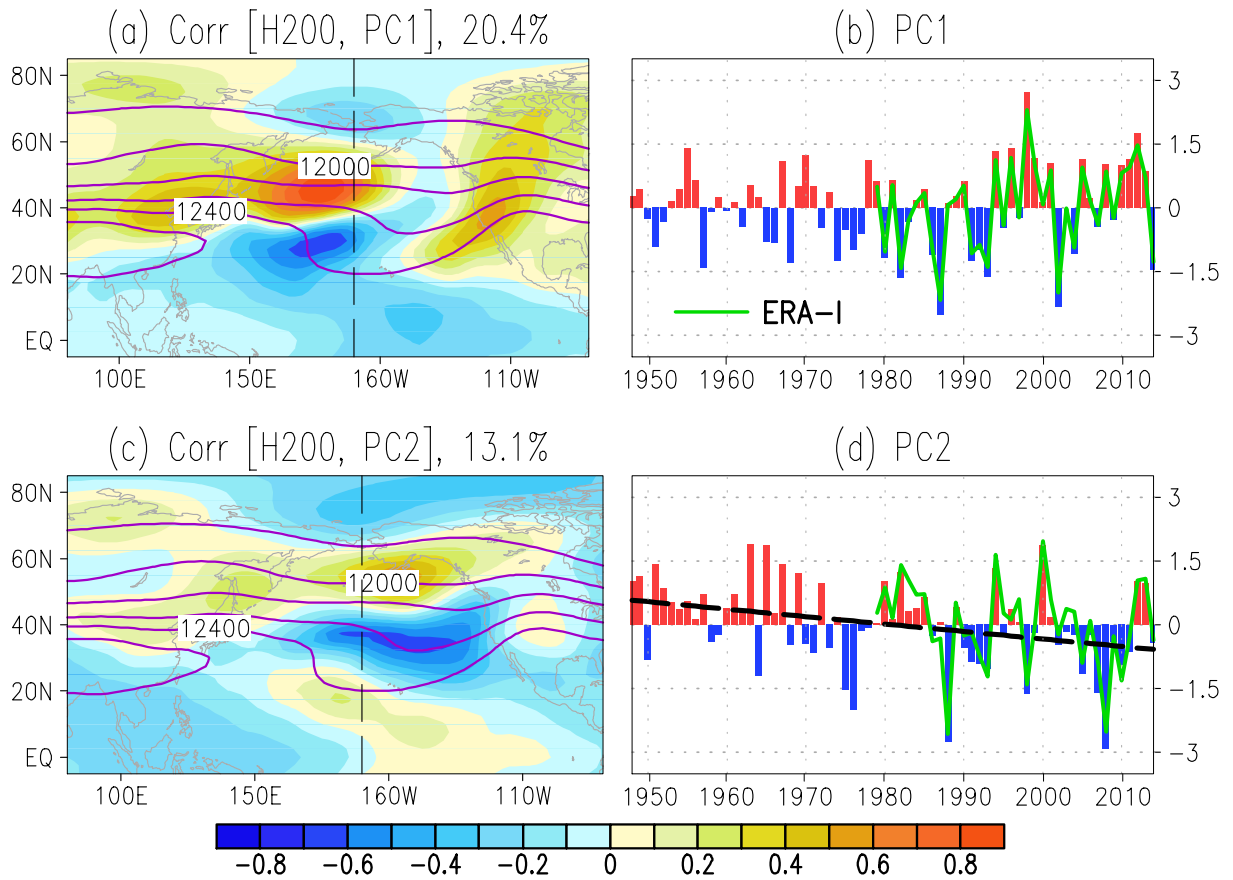
776



777

778

779 **Figure 3.** (a) Standard deviations of 200-hPa horizontal winds (Shadings), which are overlaid
 780 by climatological H200 and UV200. The blue square box outlines the domain (160°E-120°W,
 781 15°N-50°N), which is selected for a vector-EOF analysis that will be used in Fig. 4. (b)
 782 Enlargement of the blue-box domain, illustrating the frequency distribution of MPT centers
 783 and the climatological zonally asymmetric height. Each of the numbers in (b) indicates the
 784 times and locations that the MPT centers repeat.



785

786

787 **Figure 4.** The left panel depicts the correlation patterns (shadings) between H200 and the first

788 two PCs, which are overlaid by the climatological H200 (contours). The normalized PC1s and

789 PC2s are plotted in (b) and (d), respectively. The green lines in (b) and (d) indicate the PCs

790 calculated from the ERA-Interim data set. The black dashed line in (d) shows a downward

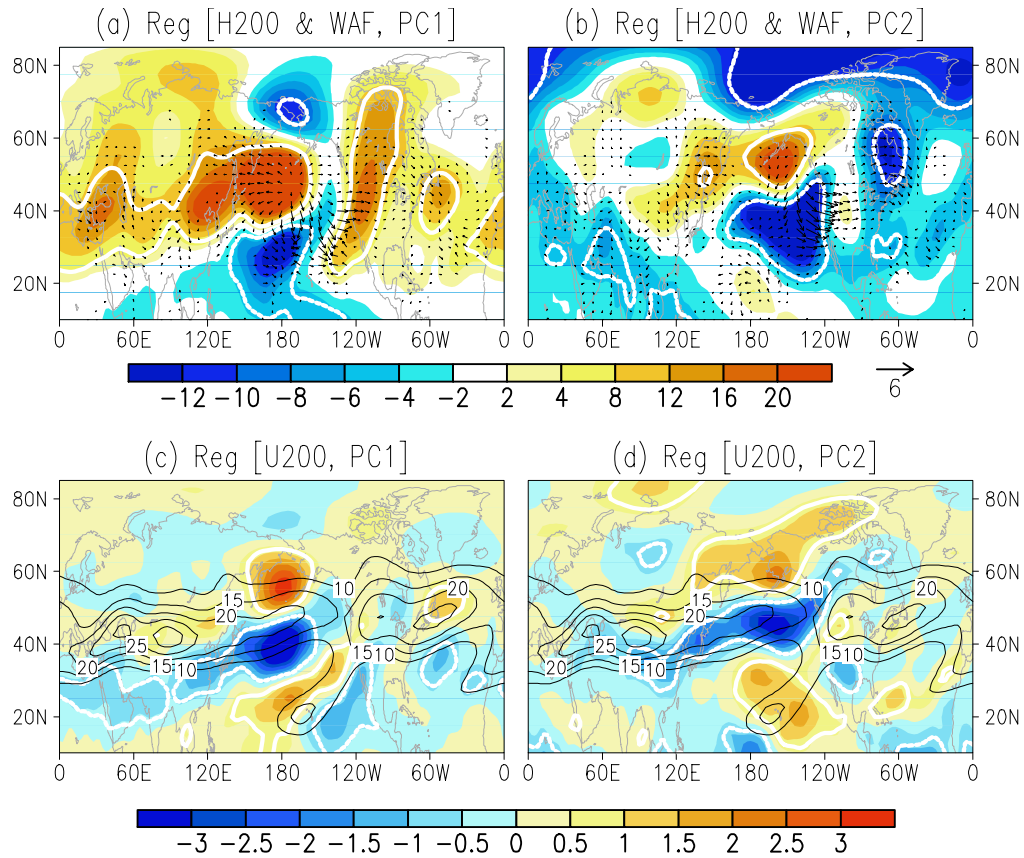
791 trend in PC2, which significantly exceeds the 99% confidence level.

792

793

794

795



796

797

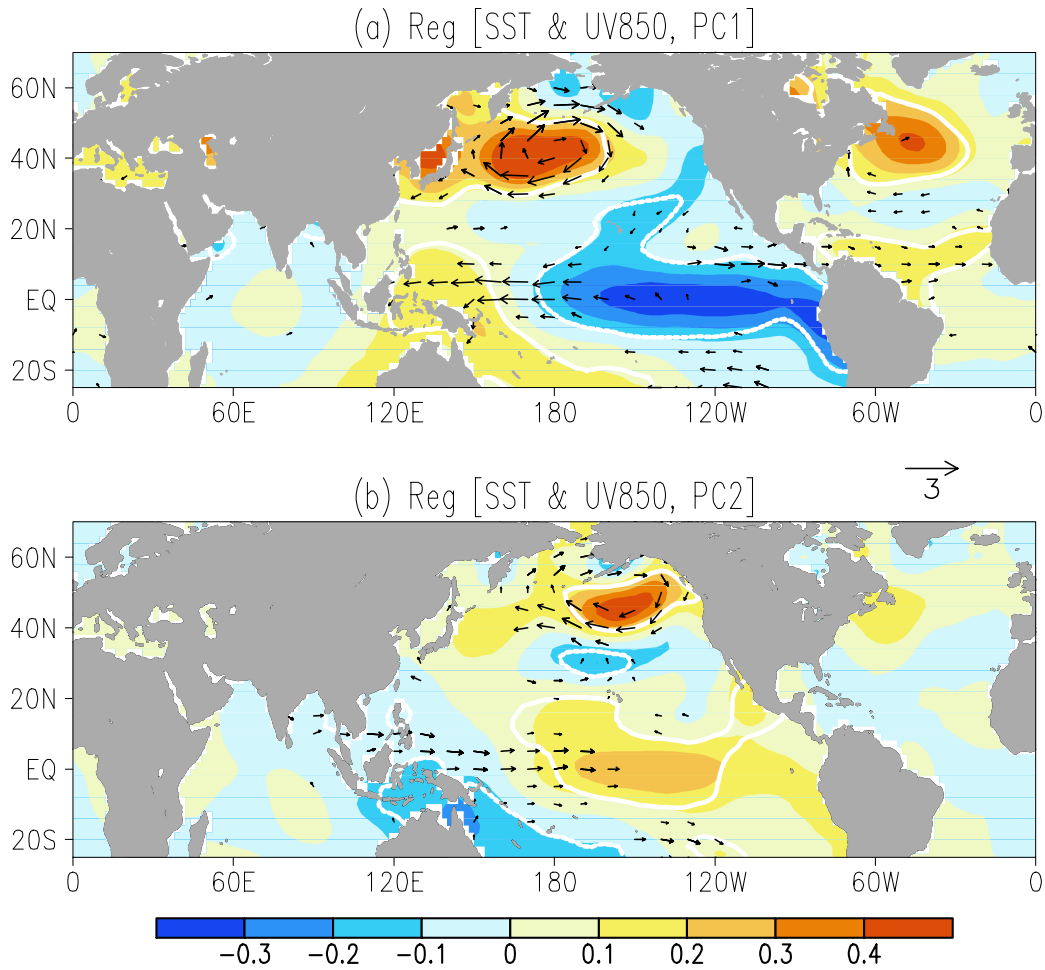
798 **Figure 5.** Regressions of H200 (shading, m) and Plumb wave activity fluxes (WAF, $m^2 \cdot s^{-2}$)

799 on PC1 (a) and PC2 (b). (c) and (d) are similar to (a) and (b) except for U200. Areas enclosed

800 by the white contours in each plot indicate the values significantly exceeding the 95%

801 confidence level. The black contours in (c) and (d) represent the climatology of U200 in JA.

802



803

804

805 **Figure 6.** Regression maps of SST and 850-hPa horizontal winds on PC1 (a) and PC2 (b).

806 Areas enclosed by the white contours present the SST anomalies exceeding the 95%

807 confidence level. Wind anomalies with a significant u or v component above the 95%

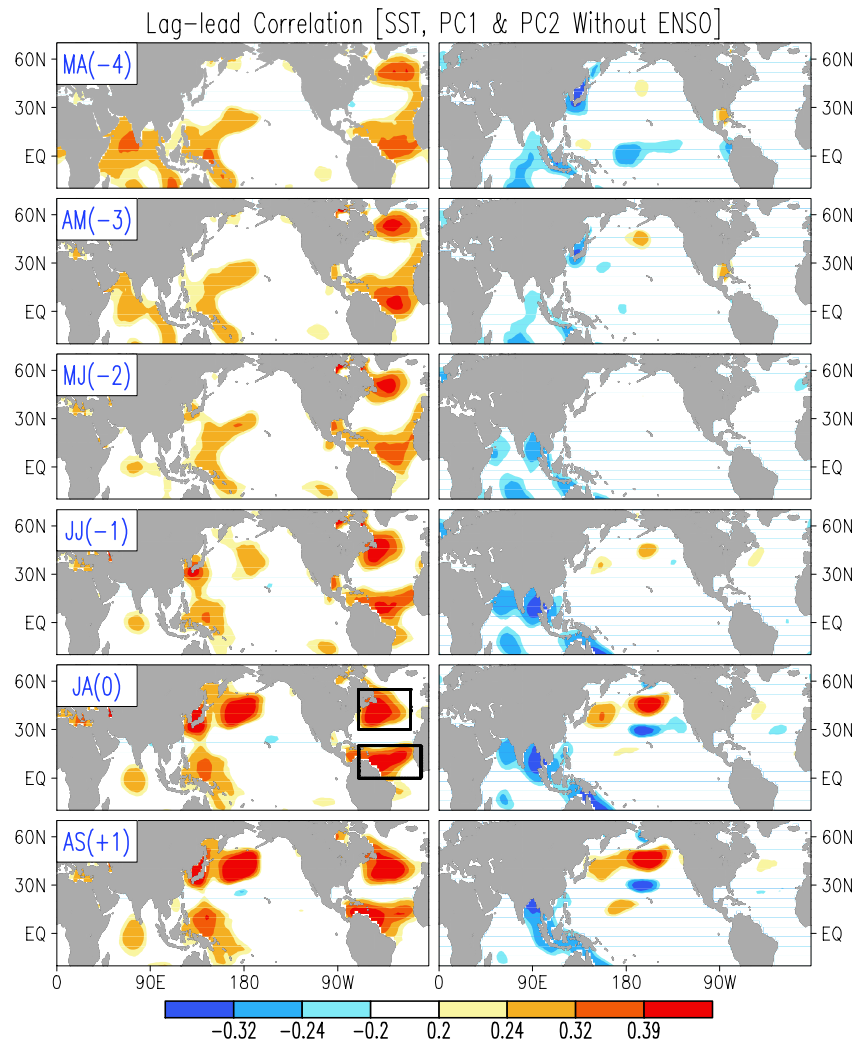
808 confidence level are plotted.

809

810

811

812



813

814

815 **Figure 7.** Lag-lead correlation maps between SST and PC1/PC2 (left/right), where the ENSO

816 signals captured by the Niño-3.4 index have been eliminated from PCs. The leading or

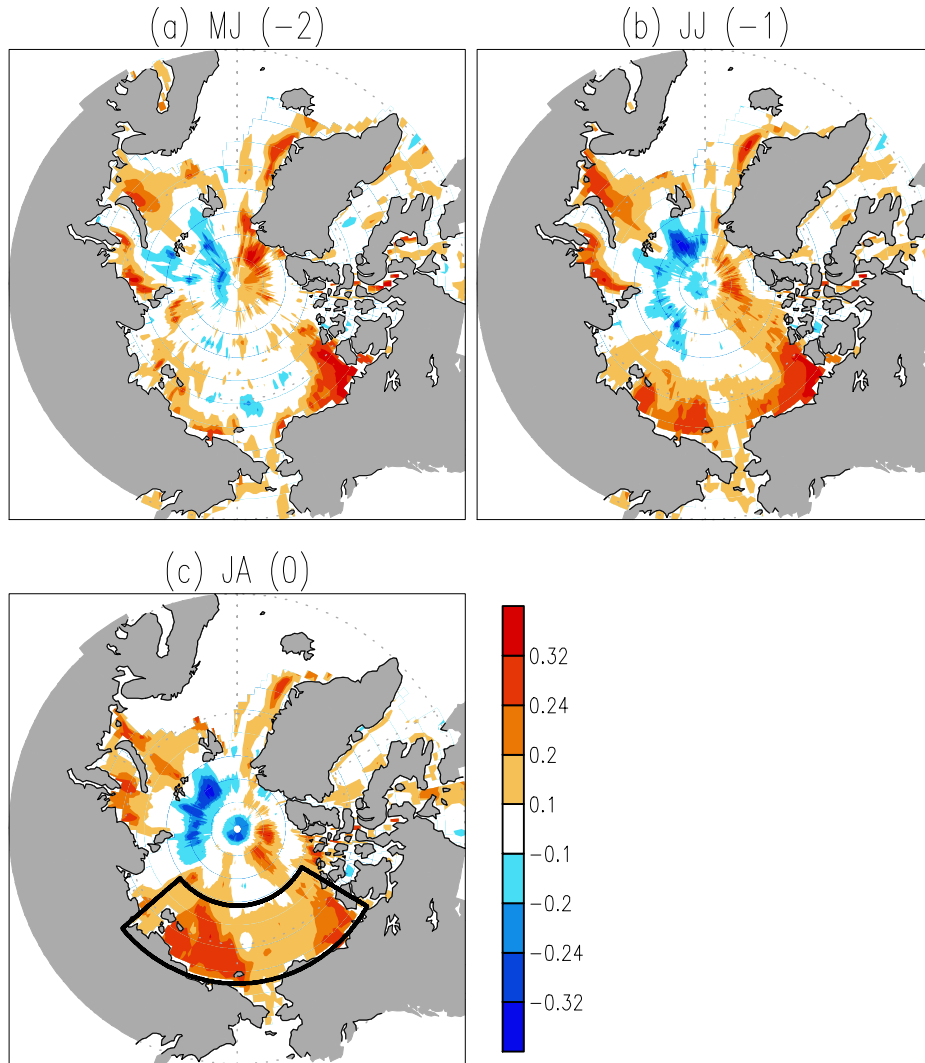
817 lagging months are labelled in each panel (e.g., -2 and -1 mean that the physical fields lead

818 the PCs by two and one months, while +1 denotes that the physical fields lag the PCs by one

819 month). The black square boxes outline the domains (70°W-10°W, 0°N-20°N; 70°W-20°W,

820 30°N-55°N) that are selected to calculate the Atlantic SST index (ASST).

821



822

823

824 **Figure 8.** Lag-lead correlation maps between the Arctic sea ice concentration and PC2, where

825 the ENSO signals captured by the Niño-3.4 index have been eliminated from PC2. Areas

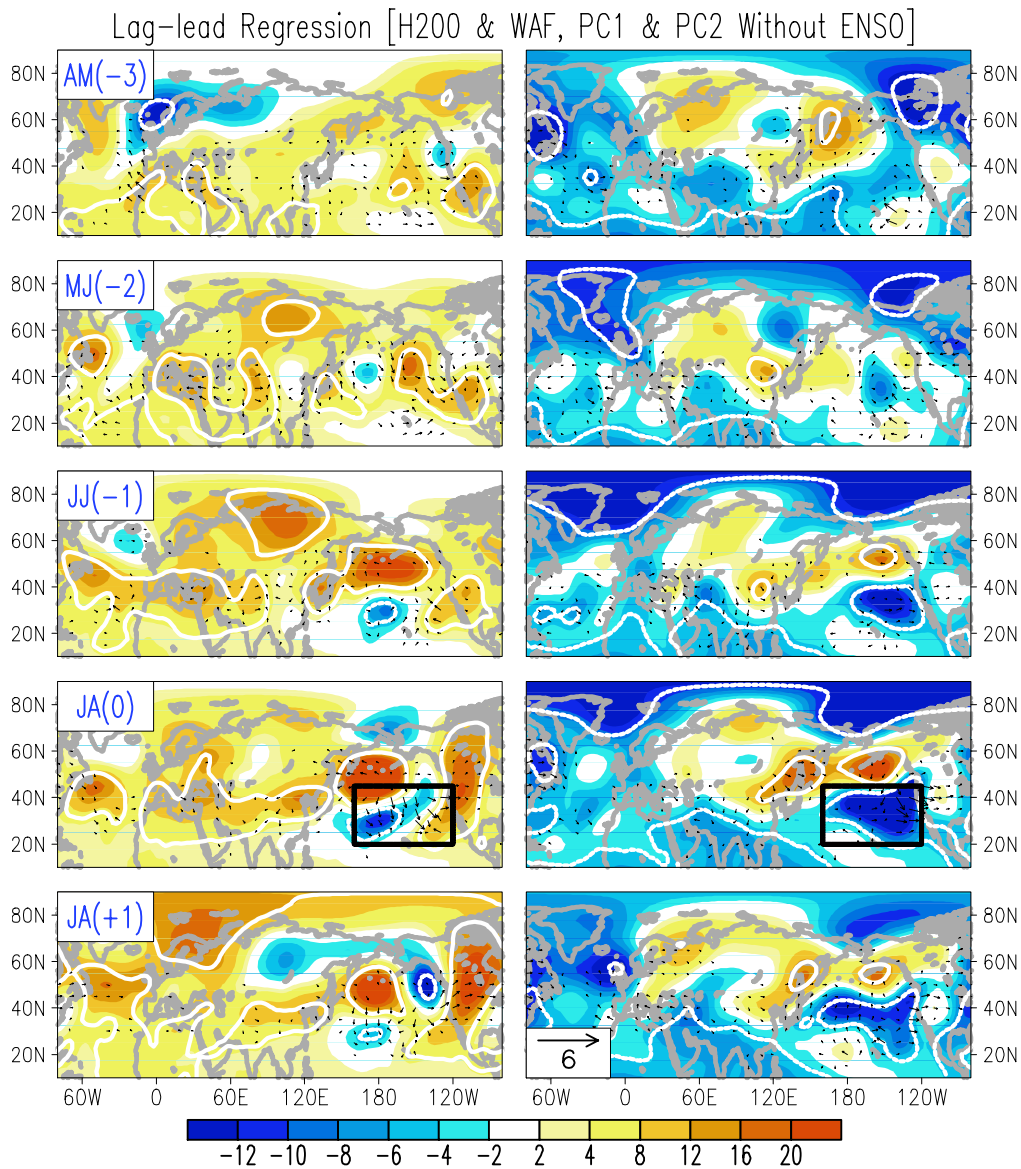
826 outlined by the enclosed lines (130°E-170°W, 70°N-80°N) are used to calculate the Arctic sea

827 ice index (ASIC).

828

829

830

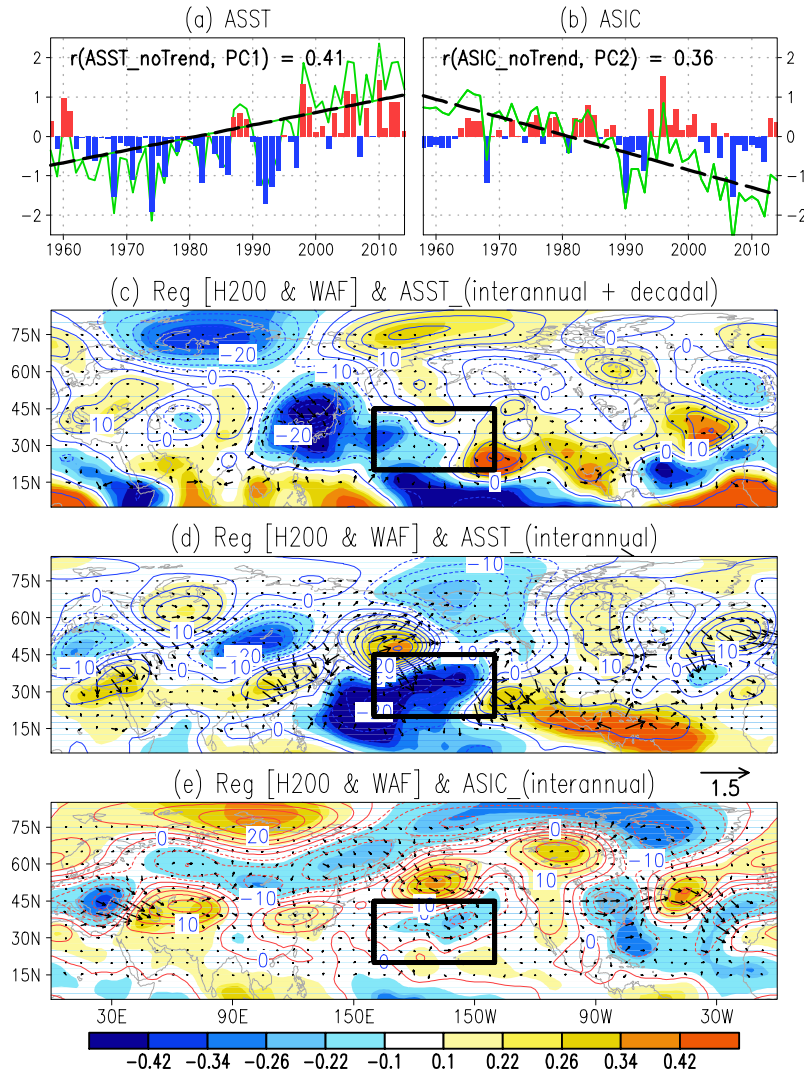


831

832

833 **Figure 9.** Lag-lead regression maps between H200 and WAF and PC1/PC2 (left/right), where
 834 the ENSO signals captured by the Niño-3.4 index have been eliminated from PCs. The
 835 leading or lagging months are labelled in each panel (e.g., -2 and -1 mean that the physical
 836 fields lead the PCs by two and one months, while +1 denotes that the physical fields lag the
 837 PCs by one month). The black square boxes indicate the climatological location of MPT.

838



839

840 **Figure 10.** Green lines in (a)–(b) show the original ASST and ASIC indices. Bars in (a) and

841 (b) indicate the residual signals after subtracting the linear trends (black lines). (c) and (e)

842 show the regression maps of H200 (contour, m) and WAF (vector, $\text{m}^2\cdot\text{s}^{-2}$) on the detrended

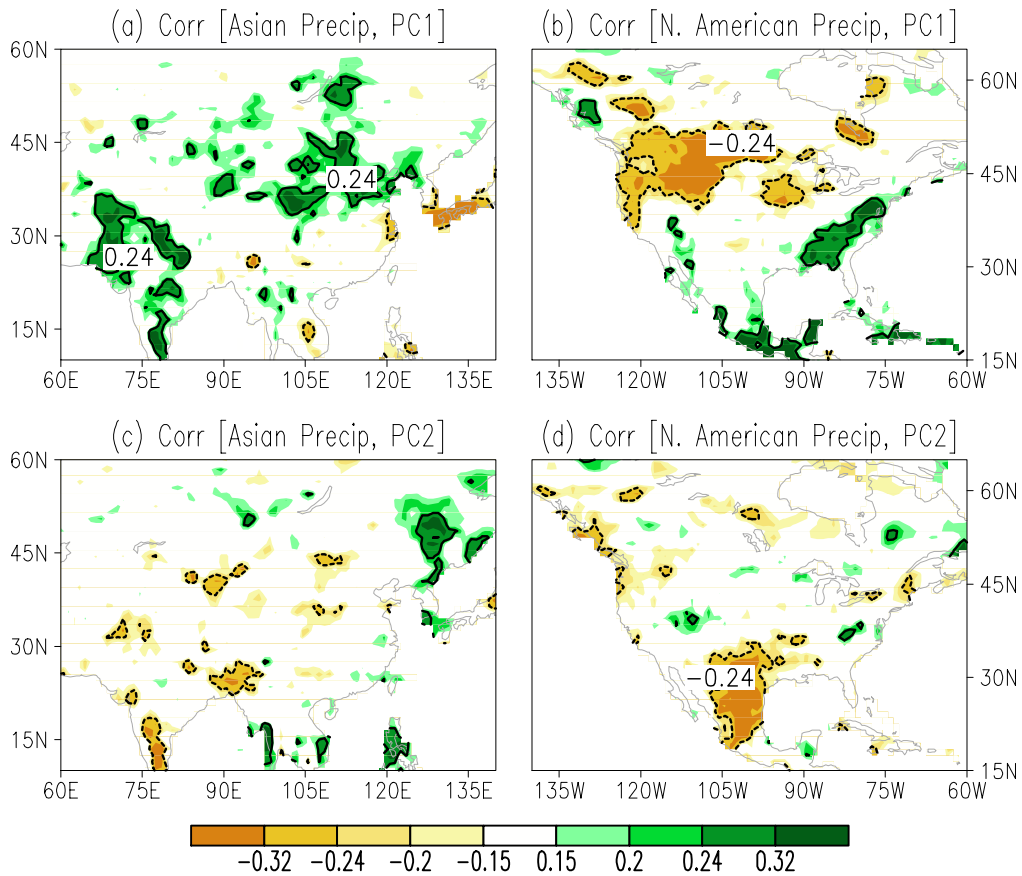
843 indices of ASST and ASIC, and (d) is similar as (a) except for regressions onto the

844 interannual variations (subtracting 9-year low filtering signals) of ASST. Shadings denote the

845 correlation coefficients between H200 and the corresponding indices. Shading values of

846 ± 0.22 , ± 0.26 , and ± 0.34 indicate the thresholds exceeding the 90%, 95%, and 99% confidence

847 levels for a degree of freedom of 55, respectively.



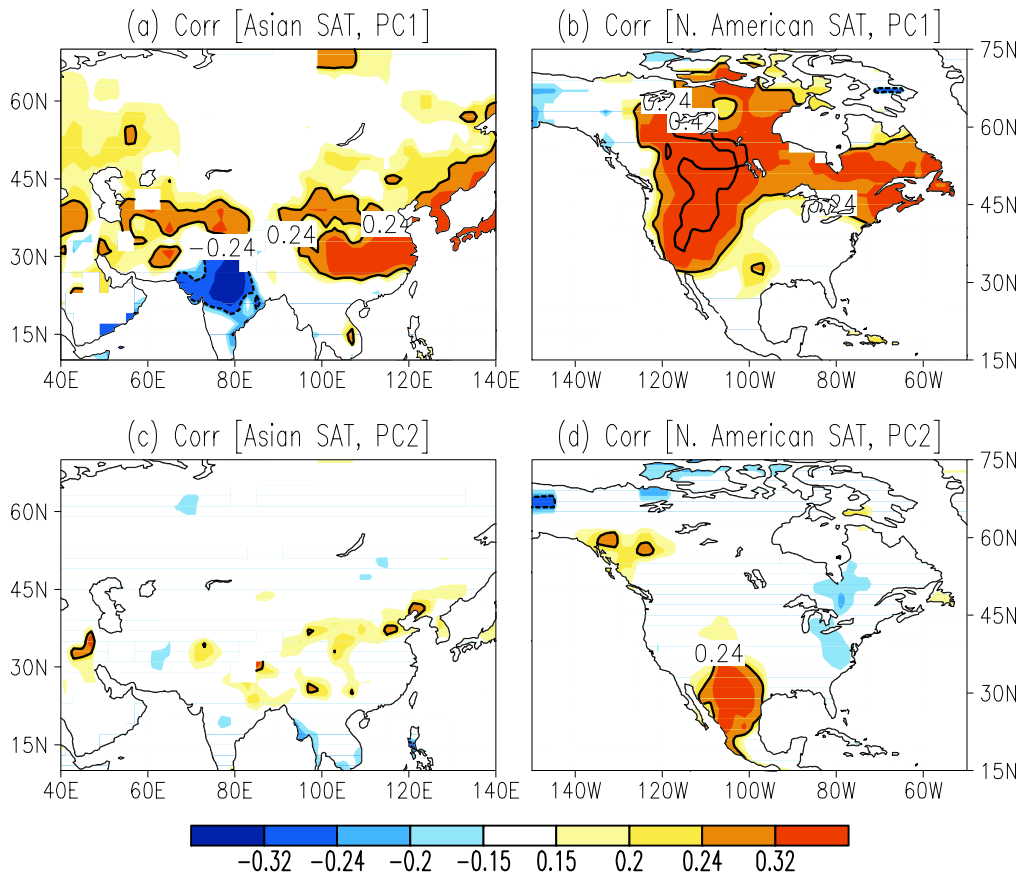
848
849

850 **Figure 11.** The upper panel shows the correlation maps between PC1 and the land
851 precipitation over Asia (a) and North America (b). The lower panel is similar to the upper
852 panel, but for the PC2. The contours values of ± 0.24 indicate the areas exceeding the 95%
853 confidence level. The linear trends have been removed from the PCs.

854

855

856



857

858

859 **Figure 12.** Same as in Fig. 10, except for the surface air temperature.

860

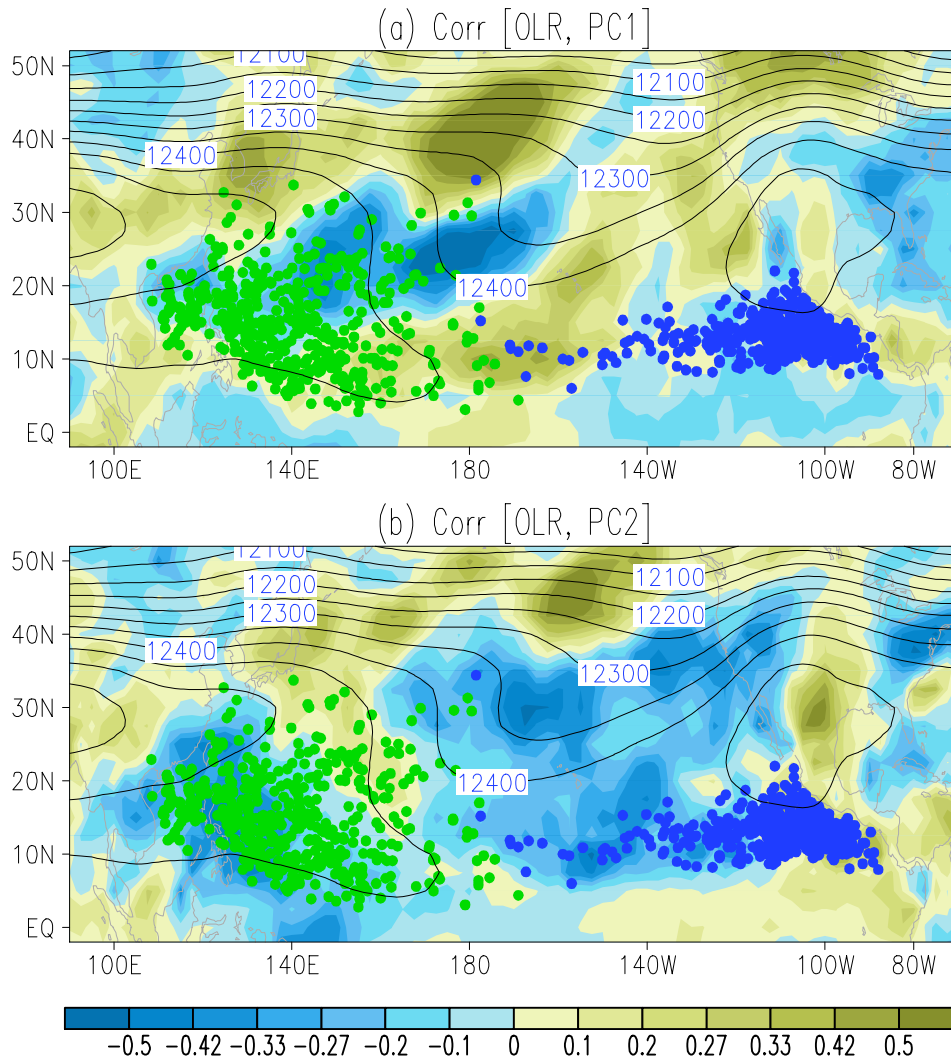
861

862

863

864

865



866

867

868 **Figure 13.** Correlation maps (shading) of outgoing longwave radiation (OLR) with PC1 (a)

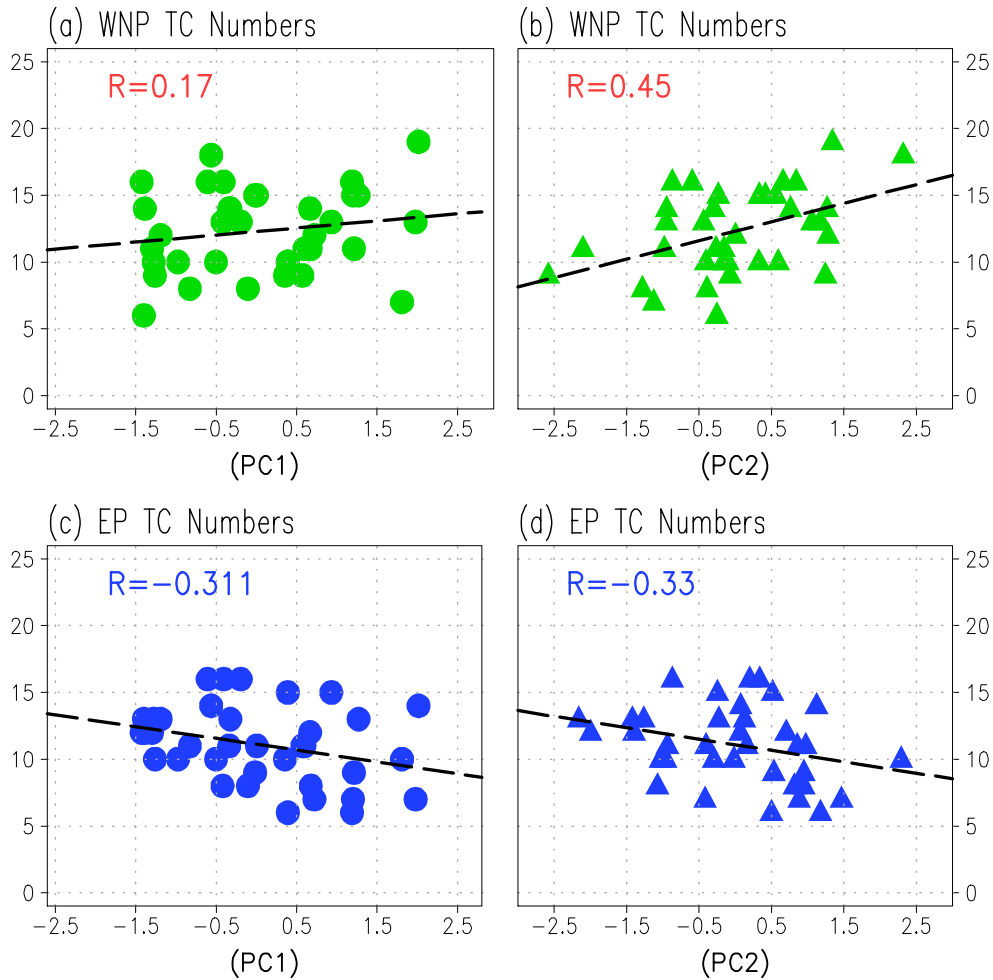
869 and PC2 (b), where ENSO signals and linear trends have been removed from the PCs. The

870 black contours represent the climatology of H20 in JA. The green and blue markers indicate

871 the genesis positions of WNP and EP tropical cyclones during boreal summer, respectively.

872

873



874

875

876 **Figure 14.** Scatter plots between TC genesis numbers and PCs, where both ENSO signals and

877 linear trends have been removed from the PCs. WNP and EP indicate the western North

878 Pacific and the eastern Pacific, respectively. The correlation coefficients between TC genesis

879 numbers and PCs are shown in each subplot.

880